

Modelling the number density of H α emitters for future spectroscopic near-IR space missions

L. Pozzetti¹, C. M. Hirata², J. E. Geach³, A. Cimatti⁴, C. Baugh⁵, O. Cucciati^{1,4}, A. Merson⁶, P. Norberg⁵, and D. Shi⁵

¹ INAF – Osservatorio Astronomico di Bologna, via Ranzani 1, 40127 Bologna, Italy
e-mail: lucia.pozzetti@oabo.INAF.it

² Center for Cosmology and Astroparticle Physics, The Ohio State University, 191 West Woodruff Lane, Columbus, Ohio 43210, USA

³ Centre for Astrophysics Research, Science and Technology Research Institute, University of Hertfordshire, Hatfield, AL10 9AB, UK

⁴ Dipartimento di Fisica e Astronomia, Università di Bologna, viale Berti Pichat 6/2, 40127 Bologna, Italy

⁵ Institute for Computational Cosmology (ICC), Department of Physics, Durham University, South Road, Durham, DH1 3LE, UK

⁶ Department of Physics and Astronomy, University College London, Gower Street, London, WC1E 6BT, UK

Received 29 July 2015 / Accepted 16 February 2016

ABSTRACT

Context. The future space missions *Euclid* and WFIRST-AFTA will use the H α emission line to measure the redshifts of tens of millions of galaxies. The H α luminosity function at $z > 0.7$ is one of the major sources of uncertainty in forecasting cosmological constraints from these missions.

Aims. We construct unified empirical models of the H α luminosity function spanning the range of redshifts and line luminosities relevant to the redshift surveys proposed with *Euclid* and WFIRST-AFTA.

Methods. By fitting to observed luminosity functions from H α surveys, we build three models for its evolution. Different fitting methodologies, functional forms for the luminosity function, subsets of the empirical input data, and treatment of systematic errors are considered to explore the robustness of the results.

Results. Functional forms and model parameters are provided for all three models, along with the counts and redshift distributions up to $z \sim 2.5$ for a range of limiting fluxes ($F_{\text{H}\alpha} > 0.5\text{--}3 \times 10^{-16}$ erg cm $^{-2}$ s $^{-1}$) that are relevant for future space missions. For instance, in the redshift range $0.90 < z < 1.8$, our models predict an available galaxy density in the range 7700–130 300 and 2000–4800 deg $^{-2}$ respectively at fluxes above $F_{\text{H}\alpha} > 1$ and 2×10^{-16} erg cm $^{-2}$ s $^{-1}$, and 32 000–48 000 for $F_{\text{H}\alpha} > 0.5 \times 10^{-16}$ erg cm $^{-2}$ s $^{-1}$ in the extended redshift range $0.40 < z < 1.8$. We also consider the implications of our empirical models for the total H α luminosity density of the Universe, and the closely related cosmic star formation history.

Key words. galaxies: evolution – galaxies: high-redshift – galaxies: star formation – galaxies: luminosity function, mass function – cosmology: observations

1. Introduction

Since the discovery of the apparent acceleration of the expansion of the Universe (e.g. Riess et al. 1998; Perlmutter et al. 1999), many efforts have been made to measure the dark energy equation of state, exploiting different observations. Among the suggestions proposed, the use of baryon acoustic oscillations (BAO) as standard rulers appears to have a particularly low level of systematic uncertainty since it corresponds to a feature in the correlation function, whereas most observational and astrophysical systematics are expected to be broad-band (e.g. Albrecht et al. 2006). Indeed, in recent years, the BAO technique has seen a dramatic improvement in capability owing to the increase in volume probed by galaxy surveys (e.g. Cole et al. 2005; Glazebrook et al. 2005; Eisenstein et al. 2005; Percival et al. 2007, 2010; Blake et al. 2011a,b; Padmanabhan et al. 2012; Xu et al. 2012; Kazin et al. 2013, 2014; Anderson et al. 2014).

The future space-based galaxy redshift surveys planned for the ESA's *Euclid* (Laureijs et al. 2011) and NASA's Wide-Field Infrared Survey Telescope – Astrophysics Focused Telescope Assets design (WFIRST-AFTA; Spergel et al. 2015b; Green et al. 2012) missions will use near-IR (NIR) slitless

spectroscopy to collect large samples of emission-line galaxies to probe dark energy. These spectroscopic surveys will identify mainly H α emitters out as far as $z \sim 2$, and their maps of large-scale structure will be used for studies of BAO, power spectrum $P(k)$ in general, large-scale structure, as well as other statistics such as the measurement of the rate of growth of structure using redshift space distortions (Kaiser 1987; Guzzo et al. 2008). In this context the space density of H α emitters (i.e. their luminosity function) is a key ingredient for a mission's performance forecast to determine the number of objects above the mission's sensitivity threshold and optimize the survey.

It is known that the cosmic star formation rate was higher in the Universe's past than it is today, possibly peaking near $z \sim 2$ (Madau & Dickinson 2014), thereby ensuring a high number of star-forming objects with high luminosity at high redshift suitable for BAO measurements. However, the abundance of H α emitters detectable by blind spectroscopy has historically been firmly established only at low redshift by means of spectroscopic surveys in the optical (e.g. Gallego et al. 1995). At higher redshift, from the ground, the intense airglow makes NIR spectroscopic searches for emission line galaxies impractical; thus systematic ground-based NIR H α spectroscopic searches

in early studies have been limited to small areas with single slit spectroscopy (e.g. Tresse et al. 2002). Therefore, narrow-band NIR searches have been used as an alternative method for identifying large numbers of $z > 0.7$ emission-line galaxies, e.g. HiZELS (Geach et al. 2008; Sobral et al. 2009, 2012, 2013) and the NEWFIRM $H\alpha$ Survey (Ly et al. 2011). These surveys have the advantage of wide area and high sensitivity to emission lines but suffer from their narrow redshift ranges and significant contamination from emission lines at different redshifts. From space, grism spectroscopy with NICMOS (Yan et al. 1999; Shim et al. 2009) and more recently with the Wide Field Camera 3 (WFC3) on the *Hubble* Space Telescope (HST), have allowed small-area surveys, such as the WFC3 Infrared Spectroscopic Parallels (WISP) survey (Colbert et al. 2013), at relevant fluxes (deeper than *Euclid* or WFIRST-AFTA) to probe the luminosity function of emission line objects at high redshift.

As a result, early studies of space-based galaxy redshift surveys often based their $H\alpha$ luminosity function models on indirect extrapolations from alternative star formation indicators such as the rest-frame ultraviolet continuum or [O II] line strength (e.g. Ly et al. 2007; Takahashi et al. 2007; Reddy et al. 2008). While physically motivated, this procedure suffers from a multitude of uncertainties in the details of the H II region parameters, dust extinction, stellar populations, and the joint distribution thereof, and the impact of uncertainties in the predicted $H\alpha$ flux is enhanced by the steepness of the luminosity function.

Motivated by the prospect of future dark energy surveys targeting $H\alpha$ emitters at NIR wavelengths (i.e. $z > 0.5$), Geach et al. (2010) used the empirical data available at that time to model the evolution of the $H\alpha$ luminosity function out to $z \sim 2$. Much more ground- and space-based data have become available since then, thanks largely to the same improvements in NIR detector technology that make *Euclid* and WFIRST-AFTA possible. In particular, the WFC3 Infrared Spectroscopic Parallels (WISP) survey (Colbert et al. 2013) has enabled the blind detection of large numbers of $H\alpha$ emitters. Due to its similarity to the observational setups planned for *Euclid* and WFIRST-AFTA, it is an excellent test case against which to calibrate expectations for these future missions.

In this work, we update the empirical model of Geach et al. (2010), collecting a larger dataset of $H\alpha$ luminosity functions from low- to high-redshift, in order to constrain the evolution of the space density of $H\alpha$ emitters. We construct three empirical models and make prediction for future $H\alpha$ surveys as a function of sensitivity threshold (i.e. counts) and redshift (i.e. redshift distributions). We scale all the luminosity functions to a reference cosmology with $H_0 = 70 \text{ km s}^{-1} \text{ Mpc}^{-1}$ and $\Omega_m = 0.3$, and present results in terms of comoving volume. The models and luminosity functions presented here are for $H\alpha$ only, *not* $H\alpha + [\text{N II}]$. The final aim of these models is to provide key inputs for instrumental simulations essential to derive forecast in future space missions, like *Euclid* and WFIRST-AFTA, that at the nominal resolution will be partially able to resolve $H\alpha$. Future simulations will clarify all the observational effects, from source confusion to the [N II] contamination and percentiles of blended lines, completeness and selection effects.

We emphasize here that our models are empirical and therefore we have reduced as much as possible any astrophysics assumption, but those based on $H\alpha$ public data. Furthermore, we do not attempt to exclude the AGN contribution from the bright end of the $H\alpha$ public luminosity functions, being AGNs valid sources (as $H\alpha$ emitters) for the current planned missions. Thus they should not be excluded to derive the total number of $H\alpha$ emitters mapped by *Euclid* and WFIRST-AFTA.

This paper is organized as follows. The input data is described in Sect. 2. The three models and the procedures used to derive them are described in Sect. 3, and the comparison to the input data is summarized in Sect. 4. Section 5 describes the redshift and flux distribution, with a focus on the ranges relevant to *Euclid* and WFIRST-AFTA, and Sect. 6 compares our results to semi-analytic mock catalogues. Our $H\alpha$ luminosity functions are compared to other estimates of the cosmic star formation history in Sect. 7. We conclude in Sect. 8. Technical details are placed in the appendices.

2. Empirical luminosity functions

Forecasts for future NIR slitless galaxy redshift surveys require as input the luminosity function of $H\alpha$ emitters ($H\alpha$ LF) in order to determine the number of objects above the mission's sensitivity threshold. In particular, we focus on the prediction for the originally planned *Euclid* Wide grism survey (Laureijs et al. 2011), i.e. to a flux limit $F_{H\alpha} > 3 \times 10^{-16} \text{ erg cm}^{-2} \text{ s}^{-1}$, and detector sensitivity $1.1 < \lambda < 2.0 \text{ } \mu\text{m}$ (sampling $H\alpha$ at $0.70 < z < 2.0$) over $15\,000 \text{ deg}^2$. A smaller area (2200 deg^2) and a fainter flux limit ($> 1 \times 10^{-16} \text{ erg cm}^{-2} \text{ s}^{-1}$) is the baseline depth of WFIRST-AFTA (Green et al. 2011) with a grism spanning the wavelength range $1.35\text{--}1.95 \text{ } \mu\text{m}$.

The original predictions presented in the *Euclid* Definition Study Report (the Red Book, Laureijs et al. 2011) used the predicted counts of $H\alpha$ emitters by Geach et al. (2010). This model was based on HST and other data available prior to 2010. Here, we provide an updated compilation of empirical $H\alpha$ LFs available in literature, and use the most recent and verified ones out to $z_{\text{max}} \sim 2.3$ to build three updated models of $H\alpha$ emitters counts. To provide precise predictions over the redshift range of interest of NIR missions (i.e. $0.7 < z < 2$) all three models include estimates from the HiZELS narrow-band ground-based imaging survey with UKIRT, Subaru and VLT (Sobral et al. 2013), covering $\sim 2 \text{ deg}^2$ in the COSMOS field at $z = 0.4, 0.84, 1.47, 2.23$; the WISP slitless space-based spectroscopic survey with HST+WFC3 (Colbert et al. 2013), sensitive to $H\alpha$ in the range $0.7 < z < 1.5$ up to faint flux levels ($3\text{--}5 \times 10^{-17} \text{ erg s}^{-1} \text{ cm}^{-2}$) on a small area ($\sim 0.037 \text{ deg}^2$); and the grism survey with HST+NICMOS by Shim et al. (2009), on $\sim 104 \text{ arcmin}^2$ over the redshift range $0.7 < z < 1.9$. To extend the models to a broader redshift range and better constrain the evolutionary form, we include other luminosity functions available at lower redshifts. Different subsets of input data are adopted in the three models to describe the evolution in redshift of the $H\alpha$ LF, as well as to explore the robustness of the predictions.

Our focus is on predictions for the yield of galaxy redshift surveys, so we work in terms of observed $H\alpha$ flux, i.e. with no correction for extinction in the target galaxy. Generally, in $H\alpha$ surveys direct measurements of extinction are unavailable, and thus require purely statistical corrections. Usually an average extinction of 1 mag. has been adopted by most of the authors (see Hopkins 2004; Sobral et al. 2013). In cases where such corrections have been applied in the literature, we have undone the correction. Furthermore, in many of the input datasets, $H\alpha$ is partially or fully blended with the [N II] doublet, and the inference of separate $H\alpha$ and [N II] fluxes is based on different assumption on their ratio or on different scaling relation. The luminosity functions presented here are for $H\alpha$ only, *not* $H\alpha + [\text{N II}]$, since future space missions, like *Euclid* and WFIRST-AFTA, will have higher spectral resolution than HST and will be partially able

Table 1. Empirical Schechter parameters for the various surveys considered, ordered by redshift.

Redshift	α	$\log_{10} L_{\star}$	$\log_{10} \phi_{\star}$	Delta-z	Area	Instr.	Reference(s)	Models
0.0225	-1.3	41.47	-2.78	0-0.045	471	prism	Gallego et al. (1995)	1,2
0.07, 0.09	-1.59	41.65	-3.14	0.02	0.24	Narrow-band	Ly et al. (2007)	1,2
0.2	-1.35	41.52	-2.56	0-0.3	0.03	CFHT	Tresse & Maddox (1998)	1,2
0.24	-1.35	41.54	-2.65	0.02	1.54	Narrow-band	Shioya et al. (2008)	1,2
0.24	-1.70	41.25	-2.98	0.02	0.24	Narrow-band	Ly et al. (2007)	1,2
0.4	-1.28	41.29	-2.4	0.02	0.24	Narrow-band	Ly et al. (2007)	1,2
0.4	-1.75	41.57	-3.12	0.02	2	Narrow-band	HiZELS (Sobral et al. 2013) ^e	1,2,3
0.6	-1.27	41.72	-2.51	0.3-0.9	0.037	HST+WF3	WISP (Colbert et al. 2013)	1,2,3
0.73	-1.31	41.97	-2.319	0.5-1.1	0.031	ISAAC	Tresse et al. (2002)	1,2
0.84	-1.56	41.92	-2.47	0.04	2	Narrow-band	HiZELS (Sobral et al. 2013) ^e	1,2,3
1.05	-1.39	42.49	-2.948	0.7-1.4	0.029	HST+NICMOS	Shim et al. (2009)	1,2,3
1.2	-1.43	42.18	-2.7	0.9-1.5	0.037	HST+WF3	WISP (Colbert et al. 2013)	1,2,3
1.25	-1.6	42.87	-3.11	0.7-1.8	0.0012	HST+NICMOS	Hopkins et al. (2000)	1,2
1.3	-1.35	42.81	-2.801	0.7-1.9	0.018	HST+NICMOS	Yan et al. (1999)	1,2,3
1.47	-1.62	42.23	-2.61	0.04	2	Narrow-band	HiZELS (Sobral et al. 2013) ^e	1,2,3
1.65	-1.39	42.55	-2.768	0.7-1.9	0.029	HST+NICMOS	Shim et al. (2009) ^c	1,2,3
2.23	-1.59	42.53	-2.78	0.04	2	Narrow-band	HiZELS (Sobral et al. 2013) ^a	1,2,3
2.23	-1.72	43.22	-3.96	0.04	GOODS-S	Narrow-band	Hayes et al. (2010) ^b	1,2
2.23	-1.6	43.07	-3.45				Hayes et al. (2010) ^c	1,2
2.23	-1.35	42.83	-3.2	0.04	0.6	Narrow-band	HiZELS (Geach et al. 2008) ^{a,d}	1,2

Notes. Units are Mpc^{-3} (ϕ_{\star}), erg s^{-1} (L_{\star}) and deg^2 (Area). ^(a) The Sobral et al. (2013) analysis includes a superset of the fields used for the earlier HiZELS paper (Geach et al. 2008). ^(b) Hayes et al. (2010) results from their internal HAWK-I data. ^(c) Hayes et al. (2010) results from a joint fit including their internal HAWK-I data and the Geach et al. (2008) data. ^(d) In the original luminosity function the ϕ_{\star} parameter quoted contains the conversion factor of $\ln 10$ (priv. comm. by authors). ^(e) We applied an aperture correction of +0.02, +0.07, +0.07, and +0.06 dex at $z = 0.40, 0.84, 1.47,$ and $2.23,$ respectively.

to resolve the H α +[N II] complex. The inferred H α luminosity function is sensitive to the prescription for the [N II] correction. In Appendix C we explore the effects of different treatments.

In Table 1 we list the compilation of H α LF Schechter parameters provided by various H α surveys spanning the redshift range $0 < z < 2$ which are used in this work. We also list the subset of data used in each model. Schechter parameters have been converted to the same cosmology and to the original H α extinguished luminosity, when necessary. The luminosities in HiZELS LFs have been further corrected for aperture. These corrections are based on the fraction of a Kolmogorov seeing disk of the specified size (0.9, 0.8, 0.8, or 0.8 arcsec, full width at half maximum, specified by Sobral et al. 2013) convolved with an exponential profile disk of half-light radius 0.3 arcsec. Similar correction has been adopted by Sobral et al. (2015a) within the same survey (see their Sect. 2.4). Variations of this procedure are explored in Appendix C, where we find a 10% change in the abundance of H α emitters in the range relevant for *Euclid* if this correction is turned off entirely, and a 2% change if the measured size-flux relation (Colbert et al. 2013) is used in place of a single reference value.

Figure 1 shows the empirical H α LFs analysed and used in our models, divided into several redshift bins from $z = 0$ (reported in all panels) to $z = 2.3$. For clarity the Schechter fits and data have been plotted only in the range of luminosities covered from each survey; the Schechter parameters have been also shown as a function of redshift (Fig. 2). Besides the H α LFs listed in Table 1 and shown in Fig. 1, we have compared fewer additional H α LFs available (Gunawardhana et al. 2013; Lee et al. 2012; Ly et al. 2011), finding that they are consistent with the data used in this work. In the highest redshift bin analysed we

further compare the observed H α LFs with the ones derived indirectly from UV in a sample of LBGs at $1.7 < z < 2.7$ (Reddy et al. 2008), finding it slightly higher than the direct observed H α LFs. Very recently new H α LFs have become available at high redshift using larger area than before, both from narrow-band imaging survey (CF-HiZELS, Sobral et al. 2015a) and using slitless spectroscopy from the analysis of a wider portion of the WISP survey (Mehta et al. 2015). Both the new H α LFs are consistent with previous determinations. In the following section we compare our models to these new data. We have not attempted instead to include in our models these new, but not independent, LFs determinations which does not reduce cosmic variance substantially and in the case of Mehta et al. (2015) and Reddy et al. (2008) have been derived indirectly from [O III] lines and UV fluxes, respectively at high- z .

From the data analysed in this work, we note that in the local Universe the shape of the H α LF is well established and characterized across a large range of luminosities (Gallego et al. 1995; Ly et al. 2007). Over the past decade, improvements in NIR grisms, slit spectroscopy, and narrow band surveys have allowed the evolution of the LF to be tracked out to $z \simeq 2$ (see references in Table 1), not only at the bright end but also below the characteristic L_{\star} . However, we note that at $z > 0.9$ the various empirical H α LFs start to disagree, as confirmed by their Schechter parameters. Despite the empirical uncertainties it is clearly evident the strong luminosity evolution of the bright end of the H α LF with increasing redshift, also confirmed by the evolution of L_{\star} by about an order of magnitudes over the whole redshift range. On the other hand, the amount of density evolution is still not completely clear, as well as the exact value and

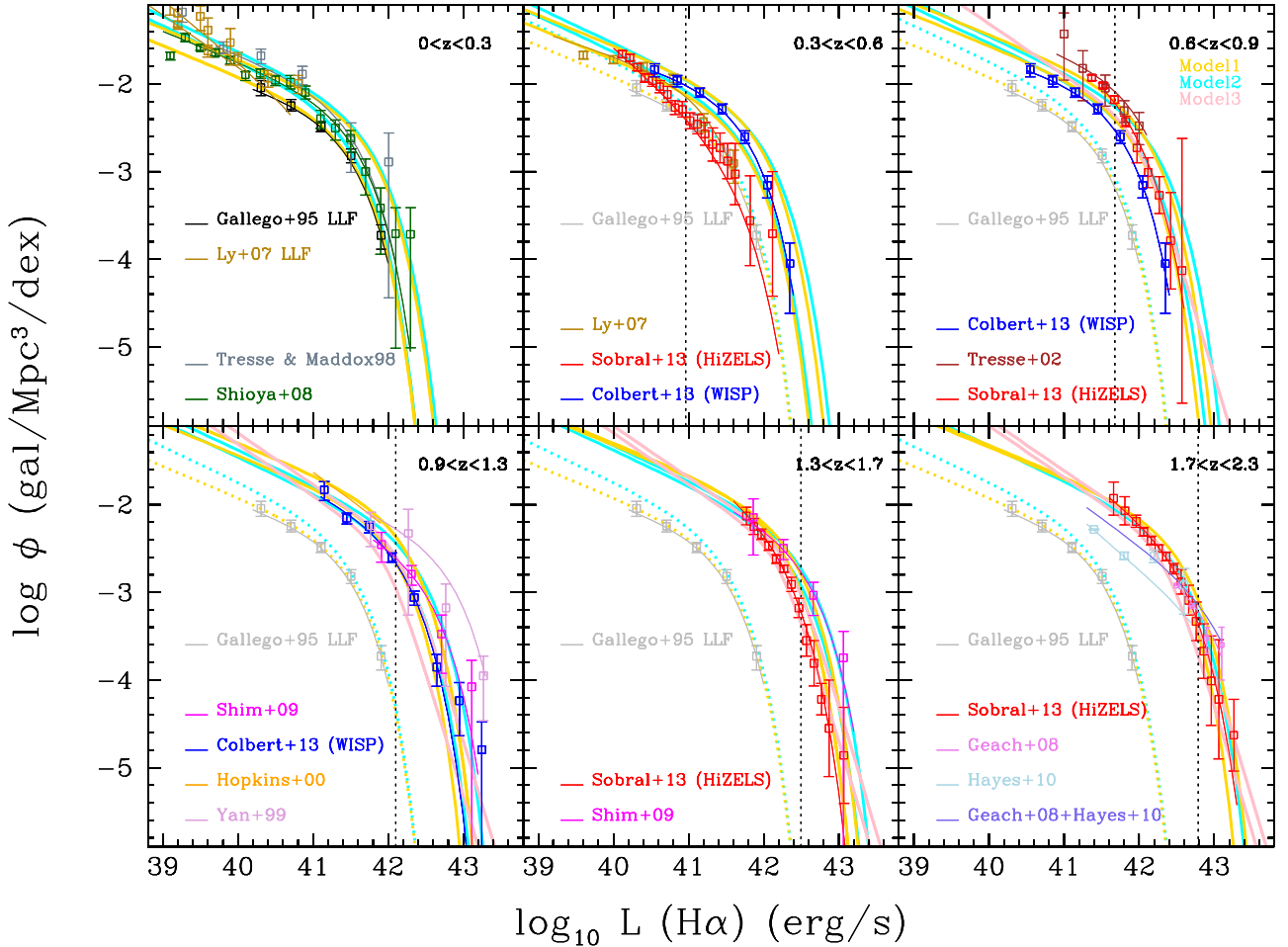


Fig. 1. $H\alpha$ LFs at various redshifts. The dotted lines mark the nominal flux limit of *Euclid* (3×10^{-16} erg cm^{-2} s^{-1}) in the lower bound of each redshift range. Observed Schechter LFs are shown as thin lines and squares in the observed luminosity range and listed in the labels. For comparison, the LFs from Empirical Models 1, 2, and 3 are shown (in yellow, cyan, and pink, respectively) as thick lines in the same redshift range (shown in the two extremes of each redshift bin).

evolution of the faint end slope, as attested by the evolution with redshift of the ϕ_* and α Schechter parameters.

3. Modelling the $H\alpha$ luminosity function evolution

As outlined in the previous section and shown in Figs. 1 and 2, in the relevant redshift range for future $H\alpha$ missions, existing $H\alpha$ LF measurements show large uncertainties and are often inconsistent with one another. In light of these uncertainties, we cannot recommend a unique model with only its statistical error associated, because this would be based on a predefined evolutionary and luminosity function shape. We, rather, present three models based on different treatments of the input data (named “Model 1”, “Model 2” and “Model 3”, hereafter). In particular we adopt three different evolutionary forms to describe the uncertain evolution of the $H\alpha$ LF. For the shape of the luminosity function, three functional forms were considered. The simplest is the Schechter function. We also adopt, different methodologies, subsets of input data, and treatment of systematic errors to explore the uncertainties and robustness of the predictions.

3.1. Model 1

In this model we used a [Schechter \(1976\)](#) parametrization for the luminosity functions and an evolutionary form similar to

[Geach et al. \(2010\)](#),

$$\phi(L, z) dL = \phi_* \left(\frac{L}{L_*} \right)^\alpha e^{-L/L_*} \frac{dL}{L_*}, \quad (1)$$

where

- ϕ_* is the characteristic density of $H\alpha$ emitters;
- α is the faint-end slope;
- L_* is the characteristic luminosity at which the $H\alpha$ luminosity function falls by a factor of e from the extrapolated faint-end power law. It has a value at $z = 0$ of $L_{*,0}$;
- and $e = 2.718\dots$ is the natural logarithm base.

We adopt the same evolutionary form for L_* assumed in [Geach et al. \(2010\)](#), and introduce an evolution in ϕ_* ,

$$L_{*,z} = L_{*,0}(1+z)^\delta \quad (2)$$

and

$$\phi_{*,z} = \begin{cases} \phi_{*,0}(1+z)^\epsilon & z < z_{\text{break}} \\ \phi_{*,0}(1+z_{\text{break}})^{2\epsilon}(1+z)^{-\epsilon} & z > z_{\text{break}}, \end{cases} \quad (3)$$

thus $\phi_{*,0}$ is the characteristic number density today, which is taken to scale as $\propto(1+z)^\epsilon$ at $0 < z < z_{\text{break}}$ and $\propto(1+z)^{-\epsilon}$ for $z > z_{\text{break}}$.

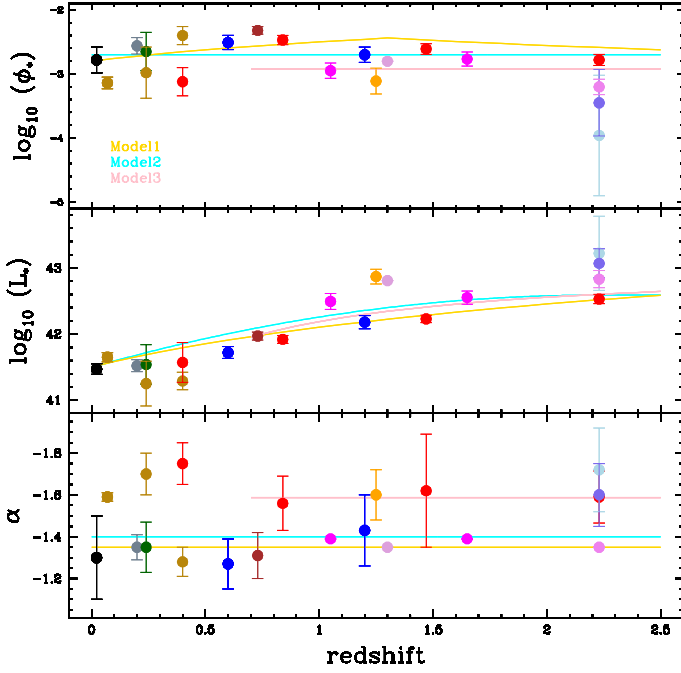


Fig. 2. H α LFs empirical Schechter parameters (using the same colours as Fig. 1) as a function of redshift (at the center redshift of each surveys), along with the evolution of parameters in the models.

Because the Schechter parameters are correlated, we do not rely on the evolution of the empirical Schechter parameters to constrain their evolution since a unique or fixed α value has not been found or fixed. We instead attempt to reproduce, by mean of a χ^2 approach, the observed luminosity functions at different luminosities and redshifts, as described by their Schechter functions in the luminosity range covered by the observations. We, therefore, find the best parameters (reported in Table 2) $\alpha = -1.35$, $L_{\star,0} = 10^{41.5}$ erg s $^{-1}$, $\phi_{\star,0} = 10^{-2.8}$ Mpc $^{-3}$, $\delta = 2$, $\epsilon = 1$, and $z_{\text{break}} = 1.3$.

3.2. Model 2

We adopt the same Schechter function for the LFs as for Model 1, but change the evolutionary form for L_{\star} as follows:

$$\log_{10} L_{\star,z} = -c(z - z_{\text{break}})^2 + \log_{10} L_{\star,z_{\text{break}}}. \quad (4)$$

In this model we normalize the evolution of L_{\star} to the maximum redshift available ($z_{\text{break}} = 2.23$) and we assume no evolution for ϕ_{\star} , i.e. $\epsilon = 0$. Using the same fitting method used for Model 1, to reproduce the observed luminosity functions at different redshift, we find the best fit parameters (reported in Table 2) $\alpha = -1.4$, $\phi_{\star,0} = 10^{-2.7}$ Mpc $^{-3}$, $c = 0.22$, $L_{\star,z_{\text{break}}} = 10^{42.59}$ erg s $^{-1}$ ($\epsilon = 0$, $z_{\text{break}} = 2.23$).

3.3. Model 3

Model 3 is a combined fit to the HiZELS (Sobral et al. 2013), WISP (Colbert et al. 2013), and NICMOS (Yan et al. 1999; Shim et al. 2009) data only. The procedure was designed specifically for use only in the redshift ranges under consideration for the *Euclid* and WFIRST-AFTA slitless surveys (in particular at $0.7 < z < 2.23$). As such, only the three largest compilations in the relevant redshift and flux range were used; in particular the low- z data is not part of the Model 3 fit and we do not display

Model 3 results at $z < 0.6$. We obtained the Model 3 luminosity function parameters and their uncertainties using a Monte Carlo Markov chain (MCMC). In Appendix C, we explore the dependence of the Model 3 fits on the assumptions, fitting methodology, and subsets of the input data used, which is a useful way to assess some types of systematic error.

Model 3 has the advantage of being fit directly to luminosity function data points, and not to the analytic Schechter fit, as done in Model 1 and 2. However, we do not recommend its use at $z \lesssim 0.6$ since it does not incorporate the low-redshift data.

A fit to the data also requires a likelihood function (or error model), in addition to central values for the data points. The luminosity functions provided by individual groups contain the Poisson error contribution, as well as estimated errors from other sources (e.g. uncertainties in the completeness correction). The construction of this model is complicated by two issues: cosmic variance and asymmetric error bars. The model for cosmic variance uncertainties is described in Appendix A. Our default fits are performed using the CV2 model, which allows for a luminosity-dependent bias. The alternative models are CV1, which assumes a luminosity-independent bias, and a no-cosmic variance model. Fitting large numbers of data points can lead to statistically significant biases if the error bars are asymmetric and this is not properly accounted for in the analysis. The treatment of asymmetric error bars is discussed in Appendix B. We use the Poisson option for our primary fits, and consider the other variations in Appendix C.

Several models for evolving luminosity functions were investigated and model parameters were fit using the MCMC. All models require a break in the luminosity function to describe the data; the break position L_{\star} is taken to be a function of redshift,

$$\log_{10} L_{\star,z} = \log_{10} L_{\star,\infty} + \left(\frac{1.5}{1+z} \right)^{\beta} \log_{10} \frac{L_{\star,0.5}}{L_{\star,\infty}}. \quad (5)$$

Where necessary, we write $L_{\star,z}$ to denote the characteristic luminosity at redshift z . For the shape of the luminosity function, three forms were considered. The simplest and most commonly used is the Schechter function, but the exponential cutoff is a poor fit to the observations. Two alternative models were considered to fix this: a hybrid model

$$\phi(L, z) = \frac{\phi_{\star}}{L_{\star}} \left(\frac{L}{L_{\star}} \right)^{\alpha} e^{-(1-\gamma)L/L_{\star}} \left[1 + (e-1) \left(\frac{L}{L_{\star}} \right)^{2\gamma} \right]^{-1} \quad (\text{hybrid}), \quad (6)$$

that mixes broken power law and Schechter behaviour; and a broken power law,

$$\phi(L, z) = \frac{\phi_{\star}}{L_{\star}} \left(\frac{L}{L_{\star}} \right)^{\alpha} \left[1 + (e-1) \left(\frac{L}{L_{\star}} \right)^{\Delta} \right]^{-1} \quad (\text{broken power law}). \quad (7)$$

The broken power law is the simplest function¹ that interpolates between a faint-end power law $\phi \propto L^{\alpha}$ and a bright-end

¹ The factor of $e-1 = 1.718\dots$ in Eq. (7) does not lead to any physical change in the model – it is equivalent to a re-scaling of the break luminosity L_{\star} . With the stated normalization, L_{\star} is the luminosity at which the LF falls to $1/e$ of the faint-end power law, which is the same meaning that it has in the Schechter function; without this factor, L_{\star} would correspond to the luminosity at which the LF falls to $1/2$ of the faint-end power law.

Table 2. Fit parameters for the three models considered.

	α	$\log_{10} \phi_{\star,0}$	$\log_{10} L_{\star,0}$	δ	ϵ	z_{break}
Model 1	$-1.35^{+0.10}_{-0.15}$	$-2.80^{+0.15}_{-0.18}$	$41.50^{+0.11}_{-0.11}$	$2.0^{+0.1}_{-0.1}$	$1.0^{+0.1}_{-0.1}$	$1.3^{+0.1}_{-0.1}$
	α	$\log_{10} \phi_{\star,0}$	$\log_{10} L_{\star,z_{\text{break}}}$	c	ϵ	z_{break}
Model 2	$-1.40^{+0.10}_{-0.15}$	$-2.70^{+0.17}_{-0.17}$	$42.59^{+0.10}_{-0.12}$	$0.22^{+0.05}_{-0.05}$	0.0	2.23
	α	$\log_{10} \phi_{\star,0}$	$\log_{10} L_{\star,2.0}$	$\log_{10} L_{\star,0.5}$	Δ	β
Model 3	$-1.587^{+0.132}_{-0.119}$	$-2.920^{+0.183}_{-0.175}$	$42.557^{+0.109}_{-0.119}$	$41.733^{+0.150}_{-0.142}$	$2.288^{+0.410}_{-0.379}$	$1.615^{+0.947}_{-1.196}$

Notes. Best fit central values and 2σ errors (without uncertainties when fixed). Units are Mpc^{-3} (ϕ_{\star}) and erg s^{-1} (L_{\star}).

power law $\phi \propto L^{\alpha+\Delta}$. Both of these models are empirically motivated: they were introduced to fit the shallower (than Schechter) cutoff at high L . We also tried an alternative functional form used for low-redshift FIR and $\text{H}\alpha$ data (Saunders et al. 1990, Eq. (1); Gunawardhana et al. 2013, Eq. (11)), however the fit is worse than for the broken power law (χ^2 is higher by 8.1, with the same number of degrees of freedom) so we did not adopt it.

The Schechter function has one fewer parameter than the others, so in this case ϕ_{\star} was allowed to have an exponential evolution with scale factor $a = 1/(1+z)$,

$$\log_{10} \phi_{\star,z} = \log_{10} \phi_{\star,1} + \frac{d \log_{10} \phi_{\star}}{da} \left(\frac{1}{1+z} - \frac{1}{2} \right), \quad (8)$$

with $(d/da) \log_{10} \phi_{\star}$ taken to be a constant. The broken power law model was used for the reference fit, since it gives the best χ^2 .

These models have $N_{\text{par}} = 6$ parameters, 3 parameters besides the standard Schechter parameters (ϕ_{\star} , α , L_{\star}), whose meaning, is as follows:

- $(d/da) \log_{10} \phi_{\star}$ (for the Schechter function) characterizes density evolution; it is positive if $\text{H}\alpha$ emitters get more abundant at late times.
- γ (hybrid model only) interpolates between an exponential or Schechter-like cutoff at high L ($\gamma = 0$) or a broken power law form ($\gamma = 1$: the power law index changes by 2 between the faint and bright ends). Values of $\gamma > 1$ are not allowed.
- Δ (broken power law model only) is the difference between bright and faint-end slopes.
- $L_{\star,z}$ has a high- z extrapolated limiting value² ($L_{\star,\infty}$) and a value at $z = 0.5$ ($L_{\star,0.5}$). The sharpness of the fall-off in L_{\star} at low redshift is controlled by β . In some models, $\log_{10} L_{\star,2.0}$ (the value at $z = 2.0$) was used instead of $\log_{10} L_{\star,\infty}$ to reduce the degeneracy with β .

The three models differ most strongly in their assumed form at the high-luminosity end: the broken power law has a power law scaling (with slope $\alpha - \Delta$), whereas the Schechter function has an exponential cutoff. The hybrid model has an exponential cutoff if $\gamma < 1$, but its steepness is decoupled from L_{\star} – as $\gamma \rightarrow 1$, the scale luminosity in the cutoff $L_{\star}/(1-\gamma)$ can be much greater than the luminosity at the break L_{\star} .

The likelihood evaluation predicts the luminosity function averaged over a bin of $\log_{10} L_{\text{H}\alpha}$ and enclosed volume $[D(z)]^3$ using $N_{\text{G}} \times N_{\text{G}}$ Gauss-Legendre quadrature scheme (for slitless surveys) or an N_{G} -point Gaussian quadrature (for

² Of course, at very high redshift the $\text{H}\alpha$ LF must fall off since there are no galaxies. We remind the reader that the empirical models built here may not be valid outside the range of redshifts spanned by the input data.

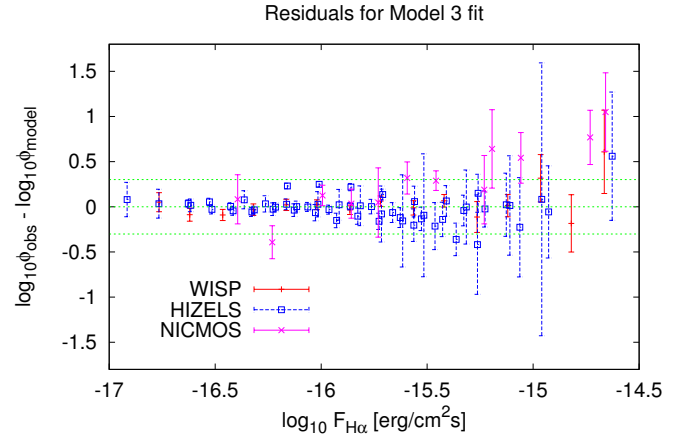


Fig. 3. Residuals to the $\text{H}\alpha$ luminosity function fits for Model 3, plotted as a function of observed-frame $\text{H}\alpha$ flux at the bin centre (horizontal axis). All redshifts are plotted together. The green lines show the fit line and factors of 2 above and below. The error bars shown do not include the cosmic variance, which is included in the fit but is highly correlated across luminosity bins.

narrow-band surveys, where there is no need to do a redshift average). The fiducial value of the quadrature parameter is $N_{\text{G}} = 3$. A flat prior was used on the 5 or 6 parameters (α , $\log_{10} \phi_{\star}$, $\log_{10} L_{\star,2.0}$, $\log_{10} L_{\star,0.5}$, β and γ or Δ , as appropriate). Chains are run with a Metropolis-Hastings algorithm; at the end a minimizing algorithm is run on the χ^2 to find the maximum likelihood model.

The best fit model (lowest χ^2) is the broken power law model with parameters (reported in Table 2) $\alpha = -1.587$, $\Delta = 2.288$, $\log_{10} \phi_{\star,0} = -2.920$, $\log_{10} L_{\star,2.0} = 42.557$, $\log_{10} L_{\star,0.5} = 41.733$, and $\beta = 1.615$ (and the corresponding $\log_{10} L_{\star,\infty} = 42.956$). The faint-end slope of $\alpha = -1.587$ is 2.0σ shallower than the ultraviolet LF slope of -1.84 ± 0.11 measured by Reddy et al. (2008), and 1.5σ shallower than -1.73 ± 0.07 measured by Reddy & Steidel (2009) at $z \approx 2$. The residuals from this fit are shown in Fig. 3.

4. Comparison to observed luminosity functions

The three empirical models constructed are plotted in Fig. 1 in different redshift bins, and compared to the observed $\text{H}\alpha$ LFs. The Schechter parameters for data and models are also shown, only for illustrative purpose, in Fig. 2. Note, however, that, since the parameters are correlated, a direct comparison between them is not straightforward, in particular Model 3 assumes also a different form for the LFs.

Given the large scatter in the observed LFs covering similar redshift ranges, all the 3 models provide a reasonable description of the data. Indeed, while it is difficult to choose a best

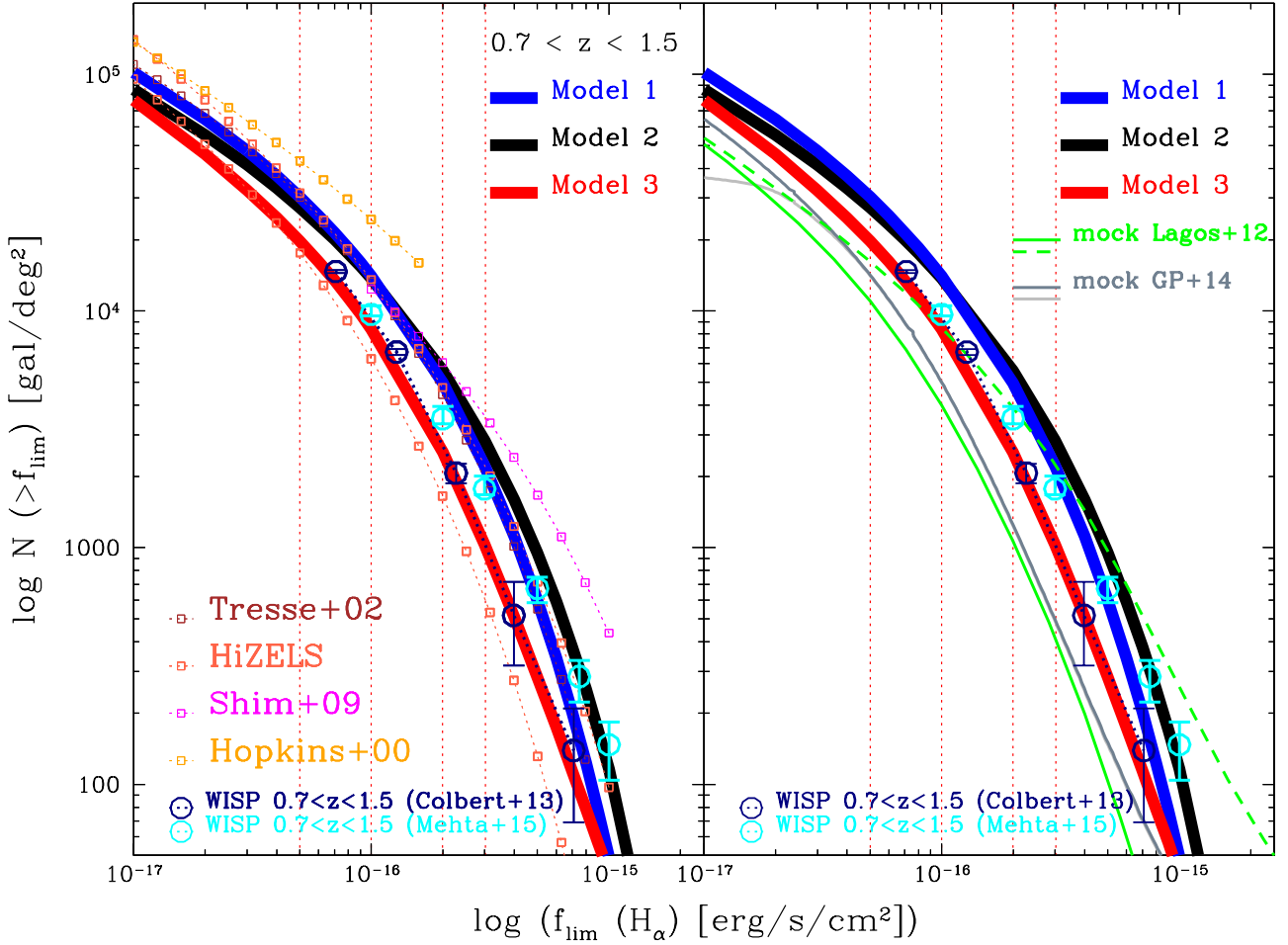


Fig. 4. *Left panel:* cumulative H α number counts, integrated over the redshift ranges $0.7 < z < 1.5$ (WISP range). The observed counts from the WISP survey (Colbert et al. 2013) are shown (blue circles) and from new WISP analysis by Mehta et al. (2015; cyan circles), and compared to the empirical Model 1, 2, and 3, (blue, black and red lines, respectively). Also shown (as dotted lines and empty squares) are the counts obtained integrating the observed LFs (see legend) in the same redshift range. *Right panel:* same cumulative H α number counts compared to the predictions from L12 mocks (green dashed and solid lines using intrinsic and extinguished H α fluxes, respectively) and GP14 mocks (dark and light grey for $H < 27$ and $H < 24$ mocks, respectively).

model, among the three, overall they describe well the uncertainties and the scatter between different observed LFs, in particular at high- z .

Comparing different redshift bins, it is evident that at low- z the models evolve rapidly in luminosity, as clearly visible also in the evolution of L_* parameter, resulting in an increase of the density of high luminosity H α emitters. Since at high- z , instead, all 3 models evolve mildly in luminosity and density, or even slightly decrease in density (for Model 1), as a consequence the density of high- L objects is almost constant.

Finally, we note that the main difference between the 3 models at all redshifts is at the bright-end of the luminosity function. Model 1 has the lower high-luminosity end, but is similar in shape to Model 2, (both assuming a Schechter form), while Model 3 has the most extended bright-end, while it is slightly lower at intermediate luminosities, and has the steepest faint-end slope. This occurs because of the different functional form used in Model 3. Current uncertainties in the bright-end of the empirical H α LFs, do not allow strong constraint on the functional form. Actually, recent analysis of GAMA and SDSS surveys (Gunawardhana et al. 2013, 2015) and of WISP (Mehta et al. 2015) suggest a LF more extended than a Schechter function but only at very bright luminosity ($>10^{43}$ erg/s). Further analysis on wider area will provide new insight on this issue.

5. Number counts and redshift distribution of H α emitters

The cumulative counts, as a function of H α flux limit, predicted by the models are shown in Fig. 4. We derive the cumulative counts in the same redshift range covered by the WISP slitless data, i.e. $0.7 < z < 1.5$. For comparison we show the observed H α WISP counts, taken from Table 2 of Colbert et al. (2013) and corrected for [N II] emission as indicated in the original paper, with $L_{H\alpha} = 0.71(L_{H\alpha} + L_{[NII]})$, for consistency with the WISP H α LF used here. Besides WISP counts, we show also the predicted counts using single luminosity functions at different redshifts (integrated over the same redshift range $0.7 < z < 1.5$). The three models reproduce well the scatter between the observed counts and observed luminosity functions, with Model 3 giving the lowest counts due to the large weight assigned to the (lower amplitude) HiZELS and WISP samples.

At the depth and redshift range of the originally planned *Euclid* Wide grism survey (Laureijs et al. 2011), i.e. $F_{H\alpha} > 3 \times 10^{-16}$ erg cm $^{-2}$ s $^{-1}$, and $1.1 < \lambda < 2.0$ μ m (sampling H α at $0.70 < z < 2.0$), Models 1, 2, and 3 predict about 2490, 3370, and 1220 H α emitters per deg 2 , respectively. This increases to 42 500, 39 700, and 28 100 H α emitters per deg 2 for

Table 3. Redshift distributions for a range of limiting fluxes (in units of 10^{-16} erg cm $^{-2}$ s $^{-1}$) from the 3 empirical Models (1, 2, 3).

Redshift	dN/dz														
	Model 1					Model 2					Model 3				
	0.5	1	2	3	5	0.5	1	2	3	5	0.5	1	2	3	5
0.0–0.1	2924	2192	1616	1339	1044	4451	3245	2329	1901	1455	–	–	–	–	–
0.1–0.2	10 252	7324	5078	4021	2909	13 491	9406	6369	4976	3543	–	–	–	–	–
0.2–0.3	17 381	11 892	7720	5768	3773	20 782	13 916	8868	6572	4267	–	–	–	–	–
0.3–0.4	23 608	15 445	9287	6511	3837	26 276	16 921	10 097	7077	4190	–	–	–	–	–
0.4–0.5	28 730	17 898	9946	6546	3462	30 255	18 731	10 475	6964	3771	–	–	–	–	–
0.5–0.6	32 705	19 372	9964	6155	2896	32 997	19 659	10 344	6543	3243	–	–	–	–	–
0.6–0.7	35 612	20 068	9570	5536	2297	34 753	19 966	9926	5987	2717	24 255	12 169	4739	2273	725
0.7–0.8	37 594	20 185	8930	4825	1757	35 731	19 840	9353	5388	2242	25 586	12 404	4517	2061	621
0.8–0.9	38 813	19 890	8164	4112	1310	36 092	19 411	8701	4794	1833	26 232	12 265	4181	1822	524
0.9–1.0	39 423	19 313	7353	3449	961	35 961	18 764	8015	4227	1487	26 290	11 831	3779	1579	437
1.0–1.1	39 561	18 553	6552	2861	698	35 430	17 959	7319	3697	1198	25 866	11 182	3350	1347	362
1.1–1.2	39 340	17 683	5794	2357	504	34 566	17 033	6627	3206	958	25 064	10 389	2923	1136	297
1.2–1.3	38 851	16 756	5097	1933	362	33 424	16 015	5946	2755	758	23 978	9514	2518	949	243
1.3–1.4	36 560	15 144	4281	1515	250	32 045	14 926	5284	2340	591	22 691	8606	2148	788	198
1.4–1.5	32 911	13 107	3447	1140	165	30 465	13 783	4642	1962	454	21 272	7703	1817	652	162
1.5–1.6	29 635	11 357	2782	861	110	28 714	12 601	4026	1619	341	19 779	6832	1528	537	132
1.6–1.7	26 704	9856	2253	654	74	26 823	11 396	3440	1311	249	18 259	6013	1279	442	107
1.7–1.8	24 090	8572	1831	499	50	24 820	10 182	2889	1038	177	16 749	5256	1067	363	87
1.8–1.9	21 760	7471	1493	382	34	22 734	8976	2378	801	121	15 277	4570	889	299	71
1.9–2.0	19 686	6527	1223	295	23	20 594	7794	1912	599	79	13 864	3954	740	246	58
2.0–2.1	17 838	5716	1006	228	16	18 430	6652	1496	432	49	12 524	3408	616	203	48
2.1–2.2	16 192	5019	830	178	11	16 275	5568	1134	298	28	11 268	2928	512	168	39
2.2–2.3	14 724	4419	689	140	7.8	14 169	4562	830	196	15	10 101	2509	427	139	33
2.3–2.4	13 412	3900	573	110	5.5	12 246	3691	594	125	7.7	9025	2147	356	115	27
2.4–2.5	12 240	3452	479	87	3.9	10 556	2969	420	78	3.8	8040	1835	298	96	22

Redshift	N														
	Model 1					Model 2					Model 3				
0.7–1.5	30 305	14 063	4962	2219	601	27 371	13 773	5588	2837	952	19 698	8389	2523	1033	284
1.5–2.0	12 188	4378	958	269	28	12 369	5095	1465	537	97	8393	2663	551	189	46
0.7–2.0	42 493	18 441	5920	2488	629	39 740	18 868	7053	3374	1049	28 091	11 052	3074	1222	330
0.9–1.8	30 708	13 034	3939	1527	317	28 225	13 266	4819	2216	621	19 995	7733	2041	779	203
0.4–1.8	48 053	22 775	8596	4244	1489	45 208	23 027	9699	5183	2002	–	–	–	–	–

Notes. Values given are dN/dz in units of deg $^{-2}$ per units redshift. Also listed the cumulative counts integrated over specific redshift ranges, in units of deg $^{-2}$. The predicted numbers include intrinsic extinction in the H α emitters and is corrected for [N II] contamination.

$F_{\text{H}\alpha} > 5 \times 10^{-17}$ erg cm $^{-2}$ s $^{-1}$ as originally planned for the Deep *Euclid* spectroscopic survey (see Table 3).

The WFIRST-AFTA mission will have less sky coverage than *Euclid* (2200 deg 2 instead of 15 000 deg 2), but with its larger telescope will probe to fainter fluxes. Its grism spans the range from 1.35–1.89 μm .³ The single line flux limit⁴ varies with wavelength and galaxy size; at the center of the wave band for a point source, and for a pre-PSF effective radius of 0.2 arcsec (exponential profile), it is 9.5×10^{-17} erg cm $^{-2}$ s $^{-1}$. The three luminosity functions integrated over the WFIRST-AFTA sensitivity curve⁵ predict an available galaxy density of 11 900, 12 400,

and 7200 gal deg $^{-2}$ (for Models 1, 2, and 3 respectively), in the redshift range $1.06 < z < 1.88$.

The previous community standard luminosity function model, used for the 2011 *Euclid* Red Book (Laureijs et al. 2011) and in pre-2012 WFIRST studies (Green et al. 2011), is that of Geach et al. (2010) divided by a factor of 1.257. This luminosity function predicts 7470 and 41 500 H α emitters per deg 2 in the same redshift range ($0.7 < z < 2$) and flux limits (>3 or 0.5×10^{-16} erg cm $^{-2}$ s $^{-1}$) of the original wide and deep *Euclid* surveys. This is a factor of about 2–6 more than estimated here at bright fluxes and a similar number at faint fluxes. The difference is partly due to the factor of $\ln 10 \approx 2.3$ from the convention for ϕ_* in the Geach et al. (2008) luminosity function, and partly because Geach et al. (2010) used the brightest and highest LF by Yan et al. (1999) as the principal constraint in the $z \sim 1.3$ range; in contrast later WISP and HiZELS samples have found fewer bright H α emitters at this redshift.

Very recently, from the new analysis by Mehta et al. (2015) of the bivariate H α -[OIII] luminosity function for the WISP survey, over roughly double the area used by Colbert et al. (2013),

³ The grism red limit was 1.95 μm in the original WFIRST-AFTA design; it was changed to 1.89 μm in fall 2014 due to an increase in the baseline telescope operating temperature.

⁴ The H α + [N II] complex is partially blended at WFIRST-AFTA resolution; the exposure time calculator (Hirata et al. 2012) now contains a correction for this effect.

⁵ Spergel et al. (in prep.). We also used the $j = 2$ galaxy size distribution in the WFIRST exposure time calculator (Hirata et al. 2012).

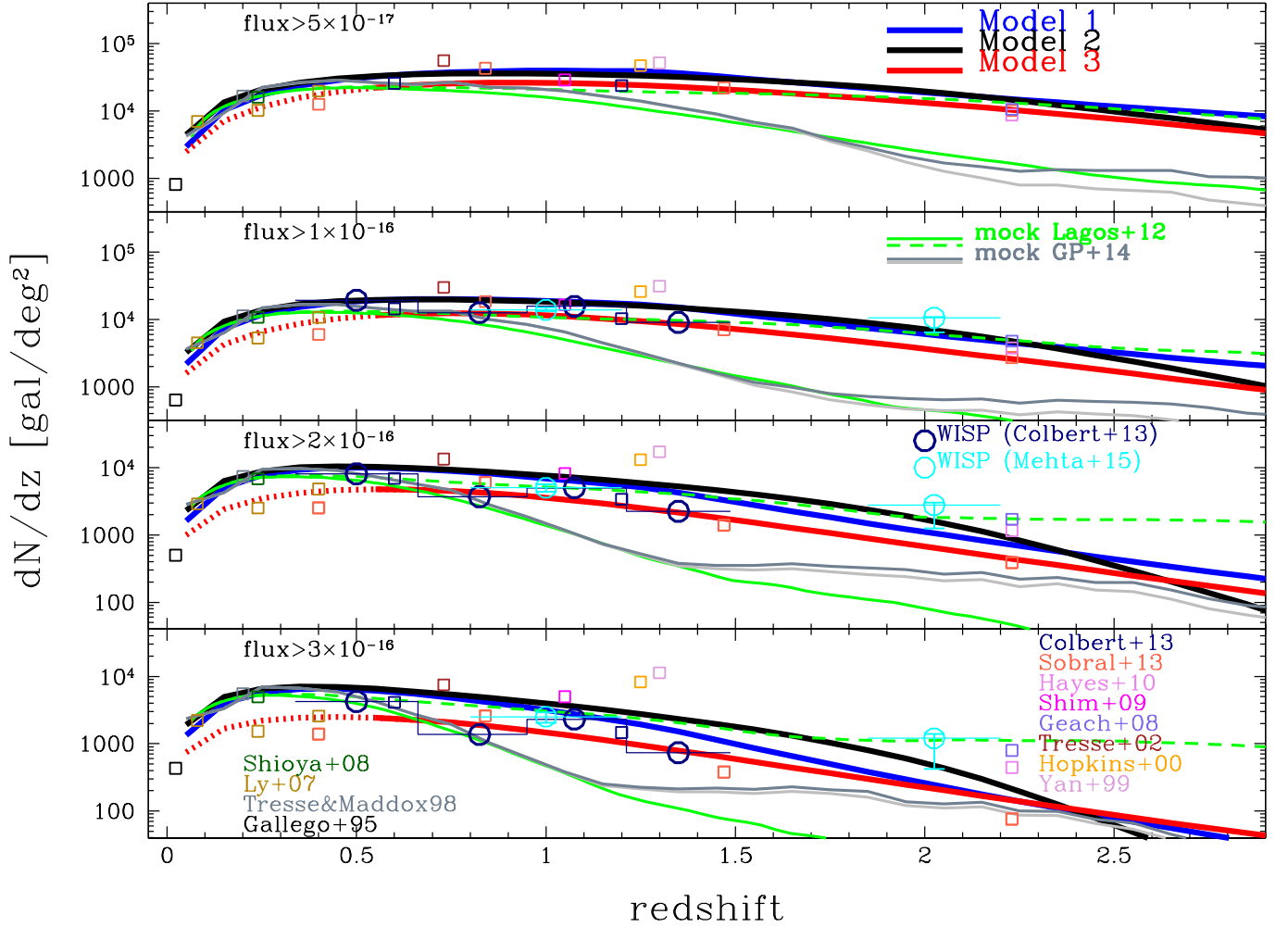


Fig. 5. H α redshift distribution above various flux thresholds (from 0.5×10^{-16} erg cm $^{-2}$ s $^{-1}$ to 3×10^{-16} erg cm $^{-2}$ s $^{-1}$, from top to bottom panels). Observed redshift distributions are indicated with open circles, while data obtained integrating LFs are shown with squares. HaLF predictions from Model 1, 2, 3 are shown as thick solid lines. The predictions from L12 mocks (green dashed and solid lines using intrinsic and extinguished H α fluxes, respectively) and GP14 mocks (dark and light grey for $H < 27$ and $H < 24$ mocks, respectively) are also shown.

they expect in the range $0.7 < z < 2$ about 3000 galaxies/deg 2 for the nominal flux limit of *Euclid* ($>3 \times 10^{-16}$ erg cm $^{-2}$ s $^{-1}$) and $\sim 20\,000$ galaxies/deg 2 for a fainter flux limit ($>1 \times 10^{-16}$ erg cm $^{-2}$ s $^{-1}$, the baseline depth of WFIRST-AFTA). We note that these expectations are more consistent with our two higher models, i.e. Model 1 and 2, than with our lowest Model 3. Fig. 4 shows their counts at $0.7 < z < 1.5$ (from their Table 4).

The redshift distributions (dN/dz) at various H α flux limits ($0.5, 1, 2, 3 \times 10^{-16}$ erg cm $^{-2}$ s $^{-1}$) relevant to the *Euclid* and WFIRST-AFTA surveys are shown in Fig. 5. Besides the observed WISP cumulative counts (from their Table 2, interpolating at the H α flux limits corrected for [N II] contamination), we show also dN/dz derived using single luminosity functions observed at different redshifts (integrated over the observed redshift range and plotted at the central redshift of each survey). It is evident that the current scatter in the observed luminosity function at $z > 1$, introduces a large uncertainty in the predictions, in particular at bright fluxes. The differences between our three models are due to the different evolution and parametrization assumed for the luminosity functions. In particular, as discussed in previous section, with Model 2 having a brighter L_* at high redshifts, the predicted dN/dz is higher at bright fluxes at $z > 1.2$. Clearly, this is a regime where large areas data are almost not available, and *Euclid* will cover this gap. At faint fluxes, instead

Model 1 and 2 are more similar, sampling the low luminosity end of their similar LFs, with Model 1 having a slightly steeper LF and higher ϕ_* . Model 3 predicts a density of emitters that is a factor from 1.5 to 2.5 lower than the other models from the faint to the bright fluxes considered, at all redshifts.

The new analysis by Mehta et al. (2015) of the WISP survey is also shown in Fig. 5. The number densities at $z \sim 2$ have been derived using the [OIII] line luminosity function, and assuming that the relation between H α and [OIII] luminosity does not change significantly over the redshift range. The expectations are quite high but consistent within the error-bars with our highest model.

In Table 3 we list the predicted redshift distributions in redshift bins of width of $\Delta z = 0.1$, at various limiting fluxes, for the three different models⁶. In addition we list also the expected numbers for the 3 models at different flux limits and in the typical redshift ranges for future NIR space missions. In particular for the original *Euclid* wide/deep surveys, designed to cover in H α the redshift range $0.7 < z < 2.0$ at flux limit about $3/0.5 \times 10^{-16}$ erg cm $^{-2}$ s $^{-1}$, using two grisms (blue+red), we expect about 1200/28 000–3400/40 000 objects for deg 2 . We

⁶ Complete tables for the 3 models at limiting fluxes from 0.1 to 100×10^{-16} erg cm $^{-2}$ s $^{-1}$ are available at <http://www.bo.astro.it/~pozzetti/Halpha/Halpha.html>

note that for the wide survey similar number densities can be reached using the same exposure time but a single grism, for example covering the redshift range $0.9 < z < 1.8$ to a flux limit of 2×10^{-16} erg cm $^{-2}$ s $^{-1}$, we expect about 2000–4800 H α emitters/deg 2 , therefore in total 30–72 million of sources will be mapped by *Euclid*. For the *Euclid* deep survey an extension of the grism to bluer wavelengths, i.e. to lower redshift, for example $0.4 < z < 1.8$, will increase the number densities to about 32 000–48 000 deg $^{-2}$ and therefore 1.3–2 million of emitters mapped in 40 deg 2 .

We remind the reader that these predictions are in terms of observed H α flux, i.e. include intrinsic dust extinction in the H α emitters, and is corrected for [N II] contamination. However, at the nominal resolution of both *Euclid* and WFIRST-AFTA, these lines will be partially blended; thus, here we may be underestimating the final detection significance of the galaxies, i.e. the sensitivity to H α flux is better than the single line sensitivity described here, even if not by the full factor of the H α :(H α + [N II]) ratio. For this reason, we expect that our analysis is somewhat conservative.

Finally, future NIR space mission will use slitless spectroscopy and therefore suffer from some degree of contamination in the spectra (depending on the rotation angles used), as well as misidentification of different emission lines, which will decrease the effective numbers of emitters available for science. We note, however, that unlike the WISP survey, both *Euclid* and WFIRST will use multiple dispersion angles to break the degeneracy in which lines from different sources at different wavelengths can fall on the same pixel. Therefore the number of objects computed from the H α LF should be reduced by the completeness factor before being used in cosmological forecasts. Preliminary estimates of this factor have been included in the *Euclid* (Laureijs et al. 2011) and WFIRST-AFTA (Spergel et al. 2015b) forecasts, and the estimates of completeness will continue to be refined as the instrument, pipeline, and simulations are developed. The problem of sample contamination depends on the abundance of other line emitters (i.e. not H α), and the data available to reject them – photometric redshifts and secondary lines. The rejection logic is specific to each survey as it depends on wavelength range, grism resolution (e.g. both *Euclid* and WFIRST-AFTA would separate the [O III] doublet), and which deep imaging filters are available. Pullen et al. (2016) present an example for WFIRST-AFTA (combined with LSST photometry) that should achieve a low contamination rate, albeit under idealized assumptions. It is presumed that deep spectroscopic training samples will be required to characterize the contamination rate in the cosmology sample. The redshift completeness factor could also be density dependent, and its estimation will require mock catalogues with clustering. The models presented here, therefore, will provide a key input to instrument simulations that aim to forecast the completeness of the *Euclid* and WFIRST-AFTA spectroscopic samples.

6. Comparison to semi-analytic mock catalogs

We compare our empirical H α models to H α number counts and redshift distributions from mock galaxy catalogues built with the semi-analytic galaxy formation model GALFORM (e.g. Cole et al. 2000; Bower et al. 2006). The dark matter halo merger trees with which GALFORM builds a galaxy catalogue are extracted from two flat Λ CDM simulations of 500 Mpc/h aside, differing only by their cosmology: (i) the Millennium simulation (Springel et al. 2005) with $\Omega_m = 0.25$, $h = 0.73$ and $\sigma_8 = 0.90$; (ii) the MR7 simulation (Guo et al. 2013) with $\Omega_m = 0.272$,

$h = 0.704$ and $\sigma_8 = 0.81$. Merson et al. (2013) provides a method for constructing lightcone galaxy catalogues from the GALFORM populated simulation snapshots, onto which observational selections can be applied, like an apparent H -band magnitude limit. These lightcones come with an extensive list of galaxy properties, including the observed and cosmological redshifts, the observed magnitudes and rest-frame absolute magnitudes in several bands, and the observed fluxes and rest-frame luminosities of several emission lines. For the present work, we have analysed lightcones built with the Lagos et al. (2012) GALFORM model⁷ (L12 mocks, hereafter) and with the Gonzalez-Perez et al. (2014) GALFORM model⁸ (GP14 mocks hereafter), using respectively the Millennium and MR7 simulations. It is essential to point out that the model parameters for Lagos et al. (2012) and Gonzalez-Perez et al. (2014) are calibrated using mostly local datasets, such as the optical and NIR galaxy luminosity functions. In particular, no observational constraints from emission line galaxies are used in the calibration process.

We are most interested in the H band magnitude and the H α flux. To assign galaxy properties, the stellar population synthesis models from Bruzual & Charlot (2003; GISSEL 99 version) is used with the Kennicutt (1983) initial mass function over the range $0.15 M_\odot < m < 120 M_\odot$. To calculate the H α flux, the number of Lyman continuum photons is computed from the star formation history predicted for the galaxy. The Stasińska (1990) models is used to obtain the line luminosity from the number of continuum photons ($T = 45\,000$ K, $n = 10$ and $N_s = 1$), testing that the choice of the HII region properties from the Stasińska models does not have an impact on the number of H α emitters. The dust extinction law is the one for the Milky Way by Ferrara et al. (1999). Broad-band magnitudes are reported on the AB scale.

In this work, we have analysed the lightcones constructed to emulate the *Euclid* surveys. In particular, in order to explore the effect of the selection on the density of H α emitters, we have explored deep mocks selected in magnitude provided on different areas (100 deg 2 limited to $H < 27$ for L12 mocks and 20 deg 2 limited to $H < 27$ or $F_{H\alpha} > 3 \times 10^{-18}$ erg cm $^{-2}$ for GP14 one).

In Fig. 4 we show the cumulative number densities derived using different mock catalogues in the redshift range $0.7 < z < 1.5$. The two lightcones, irrespective of the GALFORM version used, underpredict the cumulative counts at all H α fluxes explored (from $>10^{-15}$ up to $>10^{-17}$ erg cm $^{-2}$ s $^{-1}$), i.e. they are therefore in disagreement with the observed counts from WISP survey and with most of the counts derived from empirical LF, with the only exception of HiZELS Sobral et al. (2013). We have also tested the effect of limiting magnitudes on the H α counts from the GP14 mock, finding that a mock selected to $H < 24$ underestimates the density of H α emitters but only at very faint fluxes (3×10^{-17} erg cm $^{-2}$ s $^{-1}$).

Finally, we compare the mocks with our empirical models. We find that the mocks predict counts, in the redshift $0.7 < z < 1.5$, lower than our models; for example the GP14 mock is lower than Model 1 by a factor 2 to 4.5 from faint to bright flux limits. The L12 mock predictions are even slightly lower than the GP14 mock.

⁷ Lagos et al. (2012) *Euclid* lightcones are available from <http://community.dur.ac.uk/a.i.merson/lightcones.html>

⁸ Gonzalez-Perez et al. (2014) lightcones are available from the Millennium Database, accessible from <http://www.icc.dur.ac.uk/data/>

We have also explored the effect of dust extinction, showing the cumulative counts for intrinsic H α fluxes (i.e. before dust extinction applied) for the L12 mock in Fig. 4. In this case the simulated mock predicts very high number densities at bright fluxes ($>10^{-15}$ erg cm $^{-2}$ s $^{-1}$), above all the data available, but agree with the two faintest data from the WISP survey, which are close to the deep *Euclid* flux limit. We note that the effect of dust extinction is flux dependent in the L12 mock. However, also predictions using intrinsic H α fluxes and applying a dust extinction of 1 mag. (0.4 dex), as usually applied reversally in the data, provide counts even lower than mocks shown and flatter than our 3 models and explored data.

In Fig. 5 we further analyse the predictions for the redshift distribution, at various flux limits, from the lightcones. It is evident that redshift distribution from mocks, irrespective of the explored flux limits, are consistent with data at low redshift, while they are systematically lower than data at $z > 1$, despite the large dispersion in the data. The number densities from GP14 mock are lower than our models and data by a factor up to 10 at faint fluxes and $z > 1.5$. The L12 mock predictions are even lower than the GP14 ones, in particular at $z > 1.5$, where at all fluxes except for faint ones, the number densities continue to decrease with z and not present a flattening as in the GP14 mock. At low redshift, instead, the mocks cover relatively well the range of number densities predicted by our models, being more similar to Model 1, 2 at $z < 0.7$.

In addition, we have explored the effect of a brighter *H*-band magnitude limit ($H < 24$ compared to the original $H < 27$) in the GP14 mock, finding that it does not affect strongly the redshift distribution at all flux explored, but fainter one at high redshift ($z > 2$). Finally, we note that only using intrinsic H α fluxes, i.e. before dust extinction has been applied, the L12 mock predicts a tail in the redshift distribution at high redshift ($z > 1.5-2$) and bright flux limits consistent with our empirical models or even higher at $z > 2$ (note however that empirical models and data are not corrected for dust extinction).

We remind the reader that the SAMs used here are not calibrated using emission line datasets. The predictions of mocks for the H α LFs have been analysed by Lagos et al. (2014), see their Fig. 1). In a future work (Shi et al., in prep.), we will analyse in detail an optimization of the mocks to reproduce empirical H α LFs, taking into account also the contribution of AGN, which might affect this comparison.

7. H α luminosity density and star formation history

Finally, we consider the implications of our empirical models for the global H α luminosity density of the Universe, and the closely related cosmic star formation history.

The H α luminosity density is shown in Fig. 6, as predicted by each model. We show the total (integrating the functional form over all luminosities), along with the predictions by each model imposing flux limits at $F > 10^{-16}$ erg cm $^{-2}$ s $^{-1}$ and $F > 3 \times 10^{-16}$ erg cm $^{-2}$ s $^{-1}$. Note the excellent agreement for the integrated luminosity functions, even though the bright end is quite different for the 3 models (being lower for Model 3). As one can see from the dashed curves, the depth probed by BAO surveys picks up only a portion of the overall H α emission in the Universe: for example, Models 1, 2, and 3 predict that 31, 39, and 23 per cent respectively of the H α emission passes the flux cut $F > 10^{-16}$ erg cm $^{-2}$ s $^{-1}$ at $z = 1.5$. At $z = 1.5$, to represent half of the overall H α emission, we would need to lower the flux cut to $(3.1-6.6) \times 10^{-17}$ erg cm $^{-2}$ s $^{-1}$.

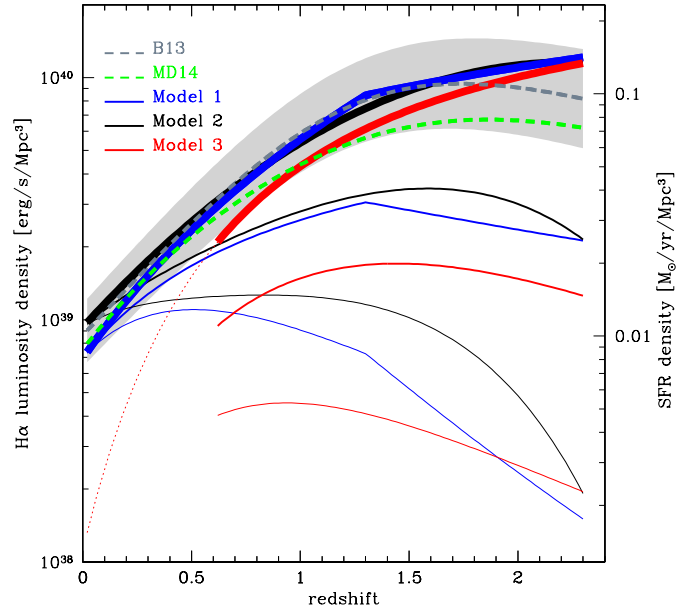


Fig. 6. H α luminosity density of the Universe as a function of redshift. The solid thick lines show the total luminosity density, whereas the thin solid curves show the luminosity density for emitters at $F > 10^{-16}$ erg cm $^{-2}$ s $^{-1}$ (upper set of curves) and $F > 3 \times 10^{-16}$ erg cm $^{-2}$ s $^{-1}$ (lower set of curves). The different colours are codes for each model (blue, Model 1; black, Model 2; and red, Model 3). Also shown is the calculation of total H α luminosity density based on the star formation histories of Madau & Dickinson (2014, green dashed) and Behroozi et al. (2013, gray dashed and shaded area). On the right axis we report also the SFR density scale for a Chabrier IMF.

Also shown in Fig. 6 is the observed (i.e. no corrected for extinction) H α luminosity density derived from the star formation history by Madau & Dickinson (2014) and Behroozi et al. (2013) along with its dispersion. We, respectively, use the conversion of $L_{H\alpha}/SFR = 7.9 \times 10^{-42}$ erg s $^{-1} M_{\odot}^{-1}$ yr (Kennicutt 1998), appropriate for a Salpeter (1955) initial mass function used by Madau & Dickinson (2014), and adding a factor of 1.7 boost, appropriate for the Chabrier (2003) initial mass function, used by Behroozi et al. (2013). For consistency, the same receipt used to correct for dust extinction in H α surveys to derive the above SFHs, has been used to correct them back, i.e. the derived H α luminosity density has been reduced by a factor of $10^{0.4}$ in accordance with the commonly-assumed 1 mag of extinction (Hopkins et al. 2004). This procedure is not an independent check, since Behroozi et al. (2013) refer to some of the same data used in this paper, but does provide an assessment of the overall consistency of the literature, particularly given that Madau & Dickinson (2014) and Behroozi et al. (2013) consider many other tracers of star formation (i.e. not just H α) as well. The agreement is within a factor of 2 difference at $z \sim 2$ for one of the star formation histories, and better for other cases – we consider this good, given the uncertainties in the extrapolation to fluxes lower than that covered by H α surveys. We further note that the agreement is still recovered if we consider a more sophisticated treatment of the dust extinction, varying it with redshift as derived from the ratio between FUV and FIR luminosity densities (Burgarella et al. 2013). However, this procedure introduces additional and uncertain assumptions on the dust extinction law and on the ratio between the extinction in the continuum and in the emission lines (Calzetti et al. 2000).

Finally, we note that on the contrary the SAMs considered in this paper predict a star formation density below the values deduced from the observations at $0.3 < z < 2$ (see Lagos et al. 2014, Fig. 3). We emphasize here that the observed/extincted $H\alpha$ luminosity density is inferred after applying a correction for dust extinction and after extrapolation down to faint unobserved $H\alpha$ luminosities, introducing therefore further uncertainties in the comparison with models.

8. Summary

The $H\alpha$ luminosity function is a key ingredient for forecasts for future dark energy surveys, especially at $z \gtrsim 1$ where blind emission-line selection is one of the most efficient ways to build large statistical samples of galaxies with known redshifts. We have collected the main observational results from the literature and provided three empirical $H\alpha$ luminosity function models. Models 1 and 2 have the advantage of combining the largest amount of data over the widest redshift range, whereas Model 3 focuses only on fitting the range of redshift and flux most relevant to *Euclid* and WFIRST-AFTA, but covered by more sparse and uncertain data.

The three model $H\alpha$ luminosity functions are qualitatively similar, but there are differences of up to a factor of 3 (ratio of highest to lowest) in the most discrepant parts of Table 3. This is despite the small aggregate statistical errors (for example ± 17 per cent at 2σ for Model 3 in the redshift range of $0.9 < z < 1.8$ and $F_{H\alpha} > 2 \times 10^{-16}$ erg cm $^{-2}$ s $^{-1}$). Some of this is due to real differences in the input datasets. In particular, our investigations of the input data in Model 3 show that minor details in the fits (such as the treatment of asymmetric error bars and the finite width of luminosity and redshift bins) as well as cosmic variance affect the outcome by more than the statistical errors in the fits. All of these models predict significantly fewer $H\alpha$ emitters than were anticipated several years ago. However, even according to our most conservative model, the upcoming space missions *Euclid* and WFIRST-AFTA will chart the three-dimensional positions of tens of millions of galaxies at $z \gtrsim 0.9$, a spectacular advance over the capabilities of present-day redshift surveys. For instance, covering the redshift range $0.9 < z < 1.8$ to a flux limit of 2×10^{-16} erg cm $^{-2}$ s $^{-1}$, we expect about 2000–4800 $H\alpha$ emitters/deg 2 , therefore in total 30–72 million of sources will be mapped over 15 000 deg 2 by the *Euclid* wide survey and 1.3–2 million of emitters will be mapped in 40 deg 2 by the *Euclid* deep survey in the range $0.4 < z < 1.8$ at fluxes above 0.5×10^{-16} erg cm $^{-2}$ s $^{-1}$. At the WFIRST-AFTA sensitivity, we predict in the redshift range $1 < z < 1.9$ about 16 to 26 million of galaxies at fluxes above $\sim 1 \times 10^{-16}$ erg cm $^{-2}$ s $^{-1}$ over 2200 deg 2 . The models presented here also provide a key input for the scientific optimization of the survey parameters of these missions and for cosmological forecasts from the spectroscopic samples of *Euclid* and WFIRST-AFTA. The $H\alpha$ LFs derived here must be folded through instrument performance, observing strategy and completeness, and modelling of the galaxy power spectrum in order to arrive at predicted BAO constraints. The previous *Euclid* forecasts (Amendola et al. 2013) are currently being updated with the new $H\alpha$ LFs and updated instrument parameters, and we anticipate that the public documents will be updated soon. The $H\alpha$ LFs presented here have already been incorporated in the most recent WFIRST-AFTA science report (Spergel et al. 2015b).

Acknowledgements. We wish to thank James Colbert, David Sobral, Lin Yan, Gunawardhana Madusha and Ly Chun for their help with the input luminosity

function data for this paper. We thank Bianca Garilli, Gigi Guzzo, Yun Wang, Will Percival, Claudia Scarlata and Gianni Zamorani to stimulate this work and for useful discussions and comments. L.P. and A.C. acknowledge financial contributions by grants ASI/INAF I/023/12/0 and PRIN MIUR 2010–2011 “The dark Universe and the cosmic evolution of baryons: from current surveys to Euclid.” C.H. has been supported by the United States Department of Energy under contract DE-FG03-02-ER40701, the David and Lucile Packard Foundation, the Simons Foundation, and the Alfred P. Sloan Foundation. This work was supported by the STFC through grant number ST/K003305/1. J.E.G. thanks the Royal Society. P.N. acknowledges the support of the Royal Society through the award of a University Research Fellowship and the European Research Council, through receipt of a Starting Grant (DEGAS-259586). C.M.B., P.N. and S.D. acknowledge the support of the Science and Technology Facilities Council (ST/L00075X/1). The simulations results used the DiRAC Data Centric system at Durham University and funded by BIS National E-infrastructure capital grant ST/K00042X/1, STFC capital grants ST/H008519/1 and ST/K00087X/1, STFC DiRAC Operations grant ST/K003267/1 and Durham University.

References

- Albrecht, A., Bernstein, G., Cahn, R., et al. 2006, ArXiv e-prints [arXiv:astro-ph/0609591]
- Amendola, L. et al. 2013, *Liv. Rev. Rel.*, 16, 6
- Anderson, L., Aubourg, É., Bailey, S., et al. 2014, *MNRAS*, 441, 24
- Behroozi, P. S., Wechsler, R. H., & Conroy, C. 2013, *ApJ*, 770, 57
- Blake, C., Davis, T., Poole, G. B., et al. 2011a, *MNRAS*, 415, 2892
- Blake, C., Kazin, E. A., Beutler, F., et al. 2011b, *MNRAS*, 418, 1707
- Bond, J. R., Jaffe, A. H., & Knox, L. 1998, *Phys. Rev. D*, 57, 2117
- Bond, J. R., Jaffe, A. H., & Knox, L. 2000, *ApJ*, 533, 19
- Bruzual, G., & Charlot, S. 2003, *MNRAS*, 344, 1000
- Burgarella, D., Buat, V., Gruppioni, C., et al. 2013, *A&A*, 554, A70
- Calzetti, D., Armus, L., Bohlin, R. C., et al. 2000, *ApJ*, 533, 682
- Chabrier, G. 2003, *PASP*, 115, 763
- Colbert, J. W., Teplitz, H., Atek, H., et al. 2013, *ApJ*, 779, 34
- Cole, S., Percival, W. J., Peacock, J. A., et al. 2005, *MNRAS*, 362, 505
- Eisenstein, D. J., Zehavi, I., Hogg, D. W., et al. 2005, *ApJ*, 633, 560
- Ferrara, A., Bianchi, S., Cimatti, A., & Giovanardi, C. 1999, *ApJS*, 123, 437
- Gallego, J., Zamorano, J., Aragon-Salamanca, A., & Rego, M. 1995, *ApJ*, 455, L1
- Geach, J. E., Smail, I., Best, P. N., et al. 2008, *MNRAS*, 388, 1473
- Geach, J. E., Cimatti, A., Percival, W., et al. 2010, *MNRAS*, 402, 1330
- Geach, J. E., Sobral, D., Hickox, R. C., et al. 2012, *MNRAS*, 426, 679
- Glazebrook, K., Baldry, I., Moos, W., Kruk, J., & McCandliss, S. 2005, *New Astron. Rev.*, 49, 374
- Green, J., Schechter, P., Baltay, C., et al. 2011, ArXiv e-prints [arXiv:1108.1374]
- Green, J., Schechter, P., Baltay, C., et al. 2012, ArXiv e-prints [arXiv:1208.4012]
- Gonzalez-Perez, V., Lacey, C. G., Baugh, C. M., et al. 2014, *MNRAS*, 439, 264
- Gunawardhana, M. L. P., Hopkins, A. M., Bland-Hawthorn, J., et al. 2013, *MNRAS*, 433, 2764
- Gunawardhana, M. L. P., Hopkins, A. M., Taylor, E. N., et al. 2015, *MNRAS*, 447, 875
- Guo, Q., White, S., Angulo, R., et al. 2013, *MNRAS*, 428, 1351
- Guzzo, L., Pierleoni, M., Meneux, B., et al. 2008, *Nature*, 451, 541
- Hayes, M., Schaerer, D., & Östlin, G. 2010, *A&A*, 509, L5
- Hirata, C. M., Gehrels, N., Kneib, J.-P., et al. 2012, ArXiv e-prints [arXiv:1204.5151]
- Hopkins, A. M. 2004, *ApJ*, 615, 209
- Hopkins, A. M., Connolly, A. J., & Szalay, A. S. 2000, *AJ*, 120, 2843
- Kaiser, N. 1987, *MNRAS*, 227, 1
- Kazin, E. A., Sánchez, A. G., Cuesta, A. J., et al. 2013, *MNRAS*, 435, 64
- Kazin, E. A., Koda, J., Blake, C., et al. 2014, *MNRAS*, 441, 3524
- Kennicutt, Jr., R. C. 1983, *ApJ*, 272, 54
- Kennicutt, Jr., R. C. 1998, *ARA&A*, 36, 189
- Lagos, C. d. P., Bayet, E., Baugh, C. M., et al. 2012, *MNRAS*, 426, 2142
- Lagos, C. d. P., Baugh, C. M., Zwaan, M. A., et al. 2014, *MNRAS*, 440, 920
- Laureijs, R., Amiaux, J., Arduini, S., et al. 2011, ArXiv e-prints [arXiv:1110.3193]
- Lee, J. C., Ly, C., Spitler, L., et al. 2012, *PASP*, 124, 782
- Ly, C., Malkan, M. A., Kashikawa, N., et al. 2007, *ApJ*, 657, 738
- Ly, C., Lee, J. C., Dale, D. A., et al. 2011, *ApJ*, 726, 109
- Madau, P., & Dickinson, M. 2014, *ARA&A*, 52, 415
- Mehta, V., Scarlata, C., Colbert, J. W., et al. 2015, *ApJ*, 811, 141
- Merson, A. I., Baugh, C. M., Helly, J. C., et al. 2013, *MNRAS*, 429, 556
- Orsi, A., Baugh, C. M., Lacey, C. G., et al. 2010, *MNRAS*, 405, 1006

- Padmanabhan, N., Xu, X., Eisenstein, D. J., et al. 2012, *MNRAS*, **427**, 2132
- Percival, W. J., Cole, S., Eisenstein, D. J., et al. 2007, *MNRAS*, **381**, 1053
- Percival, W. J., Reid, B. A., Eisenstein, D. J., et al. 2010, *MNRAS*, **401**, 2148
- Perlmutter, S., Aldering, G., Goldhaber, G., et al. 1999, *ApJ*, **517**, 565
- Pullen, A., Hirata, C., Doré, O., & Raccanelli, A. 2016, *PASJ*, **68**, 12
- Reddy, N. A., & Steidel, C. C. 2009, *ApJ*, **692**, 778
- Reddy, N. A., Steidel, C. C., Pettini, M., et al. 2008, *ApJS*, **175**, 48
- Riess, A. G., Filippenko, A. V., Challis, P., et al. 1998, *AJ*, **116**, 1009
- Salpeter, E. E. 1955, *ApJ*, **121**, 161
- Saunders, W., Rowan-Robinson, M., & Lawrence A. 1990, *MNRAS*, **242**, 318
- Schechter, P. 1976, *ApJ*, **203**, 297
- Shim, H., Colbert, J., Teplitz, H., et al. 2009, *ApJ*, **696**, 785
- Shioya, Y., Taniguchi, Y., Sasaki, S. S., et al. 2008, *ApJS*, **175**, 128
- Sobral, D., Best, P. N., Geach, J. E., et al. 2009, *MNRAS*, **398**, 75
- Sobral, D., Best, P. N., Matsuda, Y., et al. 2012, *MNRAS*, **420**, 1926
- Sobral, D., Smail, I., Best, P. N., et al. 2013, *MNRAS*, **428**, 1128
- Sobral, D., Matthee, J., Best, P. N., et al. 2015a, *MNRAS*, **451**, 2303
- Spergel, D., Gehrels, N., Baltay, D., et al. 2015b, ArXiv e-print [arXiv:1503.03757]
- Springel, V., White, S. D. M., Jenkins, A., et al. 2005, *Nature*, **435**, 629
- Stasińska, G. 1990, *A&AS*, **83**, 501
- Steidel, C., Rudie, G.C., Strom, A.L., et al. 2014, *ApJ*, **795**, 165
- Storey, P., & Zeppen, C. J., 2000, *MNRAS*, **312**, 813
- Takahashi, M. I., Shioya, Y., Taniguchi, Y., et al. 2007, *ApJS*, **172**, 456
- Tresse, L., & Maddox, S. J. 1998, *ApJ*, **495**, 691
- Tresse, L., Maddox, S. J., Le Fèvre, O., & Cuby, J.-G. 2002, *MNRAS*, **337**, 369
- Verde, L., Peiris, H. V., Spergel, D. N., et al. 2003, *ApJS*, **148**, 195
- Xu, X., Padmanabhan, N., Eisenstein, D. J., Mehta, K. T., & Cuesta, A. J. 2012, *MNRAS*, **427**, 2146
- Yan, L., McCarthy, P. J., Freudling, W., et al. 1999, *ApJ*, **519**, L47

Appendix A: Cosmic variance

This Appendix describes the treatment of cosmic variance in the Model 3 fits.

In the linear regime, the cosmic variance error covariance between two luminosity function bins i and j coming from the matter density field is given by

$$C_{ij}^{\text{CV}} = \frac{\phi(L_i)\phi(L_j)}{N_f} \int (b_i + f\mu^2)(b_j + f\mu^2) P_m(k, z) |W(\mathbf{k})|^2 \frac{d^3\mathbf{k}}{(2\pi)^3}, \quad (\text{A.1})$$

where N_f is the number of independent fields, $P_m(k, z)$ is the real-space matter power spectrum at redshift z , f is the growth rate (which boosts the cosmic variance in narrow-band surveys due to redshift-space distortions), and $W(\mathbf{k})$ is the window function, the Fourier transform of the survey volume, normalized to $W(\mathbf{0}) = 1$. We have used this result here assuming a bias of $b_i = \bar{b} = 0.9 + 0.4z$ (from a semianalytic model, Orsi et al. 2010, although there is evidence that the bias of star-forming galaxies might be higher; see e.g. Geach et al. 2012). This reduces the cosmic variance matrix to

$$C_{ij}^{\text{CV1}} = \frac{\phi(L_i)\phi(L_j)}{N_f} \int (\bar{b} + f\mu^2)^2 P_m(k, z) |W(\mathbf{k})|^2 \frac{d^3\mathbf{k}}{(2\pi)^3}. \quad (\text{A.2})$$

(Here all the entries in the covariance are constant.)

The HiZELS error bars do not incorporate a contribution from cosmic variance. However, we can estimate it from Eq. (A.1) assuming the geometry of $N_f = 2$ independent boxes of size 1×1 deg each. The depth in the radial direction is given by the width of the narrow-band filter, and is $\Delta z = 0.020, 0.030, 0.032$, and 0.032 at $z = 0.40, 0.84, 1.47$, and 2.23 respectively. The faintest bins in HiZELS at $z = 2.23$ come from the HAWK-I camera, and the survey volume is smaller in this case: it is a single field, with size 0.125×0.125 deg, and width $\Delta z = 0.046$. For the 4 redshift bins and the luminosity function bins where the full field has been observed, the implied diagonal elements of the covariance are $0.100, 0.045, 0.032$, and 0.025 . For the HAWK-I data (faintest objects at $z = 2.23$), we find a variance of 0.256 .

A more subtle issue is that the above procedure assumes that the bias is independent of $L_{\text{H}\alpha}$. This assumption has been commonly used for the purpose of forecasting H α survey performance and its dependence on survey design. However, in combination with Eq. (A.1), it implies that the cosmic variance contributions in each bin are perfectly correlated. That means that a fit using Eq. (A.1) will assume that the *shape* of the H α LF has no cosmic variance: the cosmic variance term will instead allow only the *normalization* to float up and down with an uncertainty given by Eq. (A.1). Since cosmic variance is the largest contributor to the errors in some luminosity ranges, the procedure above could lead to fit results that are artificially well-constrained, if the bias is in fact dependent on $L_{\text{H}\alpha}$. There is no reason for $db/d(\log_{10} L_{\text{H}\alpha})$ to be exactly zero, although for star-forming galaxies it is not obvious which sign to expect. We have thus explored the possibility of averaging the covariance matrix over a range of possible bias models, constrained by some kind of prior. A simple example of such a prior on the bias is that it deviates from the simple fiducial model according to a Markovian process in $\log_{10} L_{\text{H}\alpha}$,

$$\langle b_i \rangle = \bar{b}, \quad \text{Cov}(b_i, b_j) = c_1^2 \bar{b} e^{-|\log_{10} L_i - \log_{10} L_j|/c_2}, \quad (\text{A.3})$$

which results in a modified cosmic variance term⁹

$$C_{ij}^{\text{CV2}} = C_{ij}^{\text{CV1}} (1 + c_1^2 e^{-|\log_{10} L_i - \log_{10} L_j|/c_2}). \quad (\text{A.4})$$

Here c_1 is the fractional prior uncertainty in the bias and c_2 is its correlation length in $\log_{10} L$. The fiducial parameters taken are $c_1 = 0.5$ (50% scatter in the bias model) and $c_2 = 2$ (2 dex correlation length). As always with priors, these parameters are somewhat ad hoc, but despite this drawback we expect that a procedure with a range of bias models is more likely to be able to approximate the real Universe than a fixed-bias case ($C_{ij} = C_{ij}^{\text{CV1}}$) or the assumption of no cosmic variance at all.

There are thus 3 possible models for the incorporation of cosmic variance in the narrow-band luminosity function:

- No inclusion of cosmic variance ($C_{ij} = 0$).
- The simple, luminosity-independent bias model ($C_{ij} = C_{ij}^{\text{CV1}}$).
- A random suite of luminosity-dependent bias models ($C_{ij} = C_{ij}^{\text{CV2}}$).

The slitless surveys have a very different geometry: they probe tiny areas (e.g. the WFC3 detector covers only 4.8 arcmin²), but they have a very long contribution in the radial direction and usually have many more independent fields ($N_f = 29$ for WISP). For the $0.3 < z < 0.9$ and $0.9 < z < 1.5$ slices, the predicted cosmic variance diagonal covariances for WISP are 0.0020 and 0.0014 respectively. The WISP luminosity function includes the cosmic variance term, although the fitting procedure used here does not include the cosmic variance covariance between luminosity bins. We have not attempted to add these in, as the additional $\sim 4\%$ standard deviation is negligible.

Appendix B: Poisson error bars

This Appendix considers the asymmetry of the Poisson error bar in the context of constructing a likelihood function for the H α luminosity function for Model 3. The procedure was inspired by applications in cosmic microwave background data analysis, where the anisotropy power spectrum has asymmetric (in that case, χ^2 -shaped) error bars (Verde et al. 2003). A common example is in power spectrum estimation, where the overall fit can be biased downward if symmetric error bars are assumed because the lower data points have smaller error bars and pull the fit. For this reason, parameterized forms of the asymmetry are common in reporting likelihood functions in the cosmic microwave background community (see e.g. Bond et al. 1998, 2000; Verde et al. 2003). A similar phenomenon can occur in fitting a luminosity function: the Poisson error bar on a data point that fluctuates downward is smaller than on a point that fluctuates upward, so fits to the raw luminosity function that treat this error as symmetric will be biased toward lower $\phi(L, z)$. As an extreme example, the likelihood function will even allow a finite likelihood for $\phi(L, z) < 0$, which is clearly unphysical. On the other hand, treating the error on $\log_{10} \phi(L, z)$ as symmetric will bias $\phi(L, z)$ upward, since data points that fluctuate upward will have smaller error bars in log-space.

If the H α luminosity function measurements contained only Poisson errors, then the log-likelihood for a point with N objects, a survey volume ΔV , and a bin width ΔL is

$$\ln \mathcal{L} = -\ln(N!) - \lambda + N \ln \lambda, \quad (\text{B.1})$$

⁹ There are redshift-space distortion terms in Eq. (A.4) that we have neglected; we do not believe the fidelity of the model warrants a more intricate correction.

where $\lambda = \phi \Delta L \Delta V$ is the expected number of objects. The maximum likelihood point is at $\lambda = N$, and so the log-likelihood relative to the maximum is

$$\ln \mathcal{L} - \ln \mathcal{L}_{\max} = N \left(1 - \frac{\lambda}{N} + \ln \frac{\lambda}{N} \right). \quad (\text{B.2})$$

The estimate of the luminosity function is $\hat{\phi} = N/(\Delta L \Delta V)$, and the estimate of its uncertainty is $\sigma_{\ln \phi} = 1/\sqrt{N}$, so this can be re-written as

$$\ln \mathcal{L} - \ln \mathcal{L}_{\max} = \frac{1}{\sigma_{\ln \phi}^2} \left(1 - \frac{\phi}{\hat{\phi}} + \ln \frac{\phi}{\hat{\phi}} \right) = -\frac{x^2}{2\sigma_{\ln \phi}^2}, \quad (\text{B.3})$$

where we have defined the re-scaled parameter x as follow:

$$x = \pm \sqrt{2 \left(\frac{\phi}{\hat{\phi}} - 1 - \ln \frac{\phi}{\hat{\phi}} \right)}, \quad (\text{B.4})$$

with the + sign used if $\phi > \hat{\phi}$ and the - sign if $\phi < \hat{\phi}$. We note that the argument of the square root is always positive (or 0 if $\phi = \hat{\phi}$), and that x is actually an analytic function of $y = \phi/\hat{\phi} - 1$,

$$x = \pm \sqrt{2[y - \ln(1+y)]} = y - \frac{1}{3}y^2 + \frac{7}{36}y^3 - \dots \quad (\text{B.5})$$

The real error bars need not have the same asymmetry as the Poisson distribution in the cases where they are dominated by other terms (e.g. cosmic variance). We therefore test for the sensitivity of the results to the assumed fitting scheme.

The covariance matrix \mathbf{C} is re-written in terms of x , and the log-likelihood surface is taken to be quadratic,

$$\chi^2 = -2 \ln \mathcal{L} + 2 \ln \mathcal{L}_{\max} = \sum_{ij} [\mathbf{C}^{-1}]_{ij} x_i x_j. \quad (\text{B.6})$$

This approach has the advantage that with one switch in the fitting code, the error asymmetry may be treated in 4 ways:

- *Poisson*: this uses Poisson-shaped errors (Eq. (B.5)).
- *Symmetric-linear*: this uses symmetric errors in ϕ , by setting $x = y$.
- *Symmetric-log*: this uses symmetric errors in $\log_{10} \phi$ or $\ln \phi$, by setting $x = \ln(1+y)$.
- *Symmetric-native*: this uses errors symmetric in either ϕ or $\ln \phi$, depending on which was reported by the analysis team.

The Poisson shape for the error bars is probably the most realistic in the bins with small numbers of galaxies, but due to the contribution of other errors it is not exact. Therefore we consider other shapes as well (see Appendix C).

Appendix C: Variations and robustness of Model 3

In order to assess the robustness of Model 3, we re-ran the fits modifying some of the key aspects of the data handling. The reference model is based on (i) use of all datasets; (ii) the broken power law model for the luminosity function; (iii) the CV2 cosmic variance prescription; (iv) the Poisson error bar asymmetry model; (v) integration over luminosity and redshift bins using $N_G = 3$; (vi) HiZELS aperture corrections assuming a 0.3 arcsec half-light radius for all sources; and (vii) the [N II]/H α ratio assumed in the input publications. We vary the reference assumptions (functional function, CV, N_G , error bars) and we also considered extreme combinations of modifications to come up with

Galaxy counts, $1.25 < \lambda < 1.80 \mu\text{m}$, $F > 2 \times 10^{-16} \text{ erg/cm}^2/\text{s}$
Extreme combinations of variations

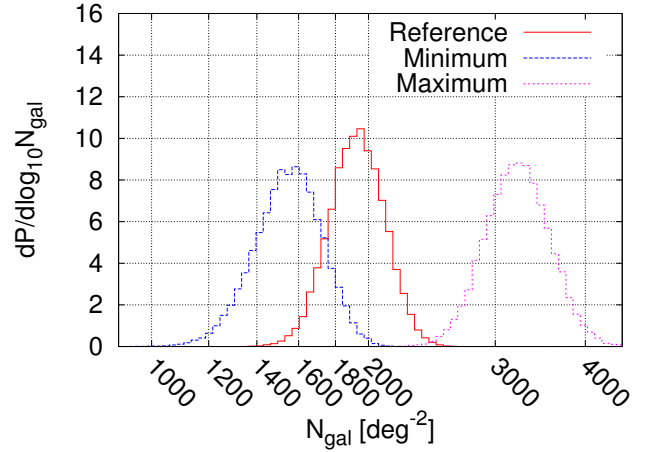


Fig. C.1. Posterior probability distribution for the number of galaxies at $F > 2 \times 10^{-16} \text{ erg cm}^{-2} \text{ s}^{-1}$ and in the wavelength range $1.25\text{--}1.80 \mu\text{m}$ (redshift $0.90\text{--}1.74$), for reference Model 3 and its extreme combinations of modifications considered (see text).

bounding optimistic (MAX) or conservative (MIN) estimates of the H α LF. Relative to the reference fit, the MAX fit used the combination of fits to the bin centre; error bars symmetric in $\log \phi$; and WISP+NICMOS data only. The MIN fit used the combination of error bars symmetric in ϕ ; and HiZELS+WISP data only. The main types of variations considered, and results of the fit are listed in Table C.1. We consider the predictions of the models for the number of galaxies N_2 above $2 \times 10^{-16} \text{ erg cm}^{-2} \text{ s}^{-1}$ and in the H α redshift range ($0.9 < z < 1.74$).

The fits with more simplistic treatment of the finite bin width (using $N_G = 1$ and the luminosity function at $z = (z_{\min} + z_{\max})/2$ and $\log_{10} L = (\log_{10} L_{\min} + \log_{10} L_{\max})/2$) lead to higher predicted counts. This is the result of Eddington-like biases: for a steeply falling luminosity function¹⁰, a bin of width $\Delta \log_{10} L \times \Delta z$ contains more galaxies than would be predicted based on the luminosity function at the bin centre. The reference fit corrects this effect by incorporating it in the model. The $N_G = 5$ case was run as a convergence test, and shows $\ll 1\sigma$ changes. The differences between the cases indicate the significance of different ways of treating finite bin size. The uncertainties are largest for the NICMOS data since large bins in both $\log L$ and z were used in the NICMOS studies (Yan et al. 1999; Shim et al. 2009). The effect of this treatment is smallest for HiZELS since there is no averaging over redshifts and the $\log L$ bins are narrow.

The choice of cosmic variance treatment (CV1 versus CV2) matters little ($\ll 1\sigma$) in the integrated counts in the *Euclid* range $F_{\text{H}\alpha} > 2 \times 10^{-16} \text{ erg cm}^{-2} \text{ s}^{-1}$ from switching between these two models, although the faint-end slope changes by 1σ .

A bigger difference arises when the cosmic variance is artificially turned off; this causes the predicted number of galaxies to go up by 2σ . This behaviour is driven by the three lowest-luminosity HiZELS points at $z = 0.84$, which have small formal error bars (0.03 or 0.04 dex) and are actually above the WISP counts.

The treatment of error bar asymmetries pulls the fits in the expected direction: treating the error bars as symmetric in ϕ leads to a lower result by almost 2σ , and treating them as symmetric in $\log_{10} \phi$ leads to a higher result by almost 2σ , relative to the

¹⁰ Technically, one with large second derivative.

Table C.1. Fit parameters for the various models considered.

		Reference parameters							
	α	Δ	$\log_{10} \phi_{\star,0}$	$\log_{10} L_{\star,2.0}$	$\log_{10} L_{\star,0.5}$	β	$\chi^2/\text{d.o.f.}$	N_2	
REF	$-1.587^{+0.132}_{-0.119}$	$2.288^{+0.410}_{-0.379}$	$-2.920^{+0.183}_{-0.175}$	$42.557^{+0.109}_{-0.119}$	$41.733^{+0.150}_{-0.142}$	$1.615^{+0.947}_{-1.196}$	64.06/76	1950^{+330}_{-330}	
		Alternate functional forms							
	α	γ	$\log_{10} \phi_{\star,0}$	$\log_{10} L_{\star,\infty}$	$\log_{10} L_{\star,0.5}$	β	$\chi^2/\text{d.o.f.}$	N_2	
hybrid	$-1.555^{+0.158}_{-0.108}$	$\star 1.000_{-0.402}$	$-2.851^{+0.206}_{-0.154}$	$42.871^{+1.125}_{-0.305}$	$41.689^{+0.136}_{-0.166}$	$1.699^{+1.071}_{-1.062}$	66.40/76	2022^{+329}_{-314}	
	α	$\log_{10} \phi_{\star,1}$	$(d/da) \log_{10} \phi_{\star,0}$	$\log_{10} L_{\star,\infty}$	$\log_{10} L_{\star,0.5}$	β	$\chi^2/\text{d.o.f.}$	N_2	
schechter	$-1.526^{+0.103}_{-0.184}$	$-2.752^{+0.124}_{-0.303}$	$-0.018^{+0.491}_{-1.297}$	$42.857^{+3.139}_{-0.277}$	$41.647^{+0.406}_{-0.138}$	$1.655^{+0.957}_{-1.425}$	83.96/76	2100^{+318}_{-341}	
		Extreme cases							
	α	Δ	$\log_{10} \phi_{\star,0}$	$\log_{10} L_{\star,2.0}$	$\log_{10} L_{\star,0.5}$	β	$\chi^2/\text{d.o.f.}$	N_2	
MIN	$-1.656^{+0.129}_{-0.106}$	$2.916^{+0.718}_{-0.598}$	$-3.039^{+0.180}_{-0.156}$	$42.583^{+0.092}_{-0.124}$	$41.772^{+0.127}_{-0.155}$	$1.698^{+1.333}_{-1.180}$	28.31/76	1596^{+283}_{-359}	
MAX	$-1.385^{+0.255}_{-0.229}$	$1.598^{+0.329}_{-0.326}$	$-2.690^{+0.322}_{-0.373}$	$42.539^{+0.245}_{-0.343}$	$41.781^{+0.271}_{-0.291}$	$\star 0.010^{+1.761}$	25.91/76	3169^{+770}_{-533}	

Notes. Central values are for the maximum likelihood model, and error ranges shown are 95 percent enclosed posterior intervals (i.e. 2σ). Of the remainder, 2.5% of the posterior is at lower values and 2.5% at higher values (except for values marked with a \star , which indicate a one-sided error bar; these are chosen where the extreme legal value of a parameter, e.g. $\beta = 0$ or $\gamma = 1$, is allowed). The final column (N_2) is the number of galaxies per square degree with an $H\alpha$ line in the range $1.25\text{--}1.80 \mu\text{m}$ with a flux exceeding $2 \times 10^{-16} \text{ erg cm}^{-2} \text{ s}^{-1}$. Units are Mpc^{-3} (ϕ_{\star}) and erg s^{-1} (L_{\star}).

Poisson-shaped error bar. The Poisson shape (reference) is the best-motivated form, since we know that a major contribution to the luminosity function error has this shape, but many past fits have been done with one of the two other shapes, and we do not have a clear understanding of the asymmetry of the systematic errors.

We performed fits excluding each of the 3 major input samples. Since the narrow-band HiZELS $H\alpha$ luminosity function is the lowest in the *Euclid* range, and the NICMOS results are the highest, exclusion of HiZELS moves the predicted number of galaxies up, whereas exclusion of NICMOS moves it down. The difference between the highest and lowest result in this sample jack-knife is 0.161 dex. This suggests that systematic errors are contributing to the differences of these curves and that caution should be exercised in interpreting joint fits.

The alternative fitting functions, especially the Schechter function, lead to slightly greater number densities than the reference (broken power law). This is because they incorporate an exponential cutoff, and hence the existence of a few very bright galaxies ($>5 L_{\star}$, particularly in the NICMOS data) pulls the characteristic luminosity to larger values and increases the number of objects in the intermediate range ($\sim 2 L_{\star}$). However, this same feature of the Schechter law means that it is a poor fit to the NICMOS observations, and it is disfavoured relative to the broken power law model by $\Delta\chi^2 = 20$, and in any case the effect in our fiducial range ($F_{H\alpha} > 2 \times 10^{-16} \text{ erg cm}^{-2} \text{ s}^{-1}$, $0.90 < z < 1.74$) is only 1σ .

The reference aperture correction for HiZELS assumes a half-light radius of 0.3 arcsec, which is consistent with objects near the flux limit of WFIRST-AFTA (see Colbert et al. 2013, Fig. 11). We have tried two variations on this: an extreme case of turning the aperture correction off, and a case of implementing a variable galaxy size in accordance with the fit provided in Sect. 4.2 of Colbert et al. (2013)¹¹. The changes

in the number of objects in the range $0.90 < z < 1.74$ and at $F_{H\alpha} > 2 \times 10^{-16} \text{ erg cm}^{-2} \text{ s}^{-1}$ are -10% and -2% for the no aperture correction and Colbert et al. (2013) correction cases, respectively.

The last modelling assumption that was varied was the assumed $[\text{N II}]/H\alpha$ ratio, which enters because at low resolution $[\text{N II}]$ and $H\alpha$ are blended; thus $H\alpha + [\text{N II}]$ is measured, and $H\alpha$ is inferred under some assumed prescription for the line ratio. The reference model is based on the $H\alpha$ luminosity function directly from the published papers: this means that the assumed $[\text{N II}]/H\alpha$ is that in the published papers (0.41 for NICMOS and WISP; in HiZELS a variable ratio was used but the reported median is 0.33). Here $[\text{N II}]$ includes both doublet members, 6548 \AA and 6583 \AA ; 75.4% of the flux in the stronger 6583 \AA line (Storey & Zeppen 2000). This ratio is common at low redshifts, however a range of values is observed, and in high-redshift galaxies the $[\text{N II}]/H\alpha$ ratio is often observed to be smaller. We have therefore investigated what happens under alternate assumptions regarding the $[\text{N II}]/H\alpha$ ratio. First, the luminosities were converted back to $L_{H\alpha + [\text{N II}]}$ using the stated median ratios in each input paper. Then the $H\alpha + [\text{N II}]$ luminosity function was written as

$$\phi_{H\alpha + [\text{N II}]}(L_{H\alpha + [\text{N II}]}) = \int \phi_{H\alpha}(L_{H\alpha}) p(x|L_{H\alpha}) \left. \frac{\partial L_{H\alpha}}{\partial x} \right|_{L_{H\alpha + [\text{N II}]}} dx, \quad (\text{C.1})$$

where $x = \log_{10}(L_{6583}/L_{H\alpha})$ is the relative line strength in dex and $L_{H\alpha} = L_{H\alpha + [\text{N II}]}/(1 + 10^x/0.754)$. We built two alternative models for the $[\text{N II}]/H\alpha$ ratio based on the $\langle z \rangle = 2.3$ BPT diagram of star-forming galaxies (Steidel et al. 2014). One model (a1tNII1) uses the median $[\text{N II}]/H\alpha$ ratio from the Steidel et al. (2014) sample, $x = -0.90$ dex (see Fig. 5). The other (a1tNII2) assumes a lognormal distribution; since the 84th percentile ($+1\sigma$) of the $[\text{N II}]/H\alpha$ ratio corresponds to $x = -0.57$ dex, we choose a median at -0.90 dex and a scatter of $\sigma_x = 0.33$ dex.

In the a1tNII1 model, the number of objects in the range $0.90 < z < 1.74$ and at $F_{H\alpha} > 2 \times 10^{-16} \text{ erg cm}^{-2} \text{ s}^{-1}$ increases

¹¹ For this fit, the $H\alpha$ luminosities were re-scaled, and the differential luminosity function was appropriately transformed using the Jacobian of the uncorrected-to-corrected flux transformation.

by 45%; the weaker assumed [N II] results in larger inferred H α luminosities, and this effect is amplified by the steep luminosity function. On the other hand, for the `altNII2` model, which includes scatter as well, we find a source density only 29% above the reference model; the reduction occurs because the scatter in [N II] results in an Eddington-like bias that is corrected by Eq. (C.1). While an improvement over the reference model in some ways, the 29% increase in the `altNII2` model may be an overestimate, since (i) it applies a correction based on the $\langle z \rangle = 2.3$ BPT diagram even at lower redshifts; and (ii) the correction procedure is not technically correct for HiZELS,

which has a variable assumed [N II] fraction and which may include only part of the H α + [N II] complex in its band¹². There may also be differences (whose impact has undetermined sign) between the rest-frame ultraviolet selection in Steidel et al. (2014) and H α selection. Based on these considerations, we are not using it to replace the reference model.

Finally, it is seen that the central values of the MIN and MAX fits for the number of objects in the range $0.90 < z < 1.74$ and at $F_{\text{H}\alpha} > 2 \times 10^{-16} \text{ erg cm}^{-2} \text{ s}^{-1}$ differ by a factor of 2 (see Table C.1).

¹² The correction in Eq. (C.1) is an overestimate in cases where H α falls in the narrow bandpass and one or both of the [N II] lines do not. It is an underestimate if [N II] 6583 Å falls in the narrow band and H α does not, but since H α is almost always stronger this is not as much of an issue at the top of the luminosity function.